ChemPubSoc Europe

DOI: 10.1002/cphc.201300259

The Registry Index: A Quantitative Measure of Materials' Interfacial Commensurability

Oded Hod*[a]

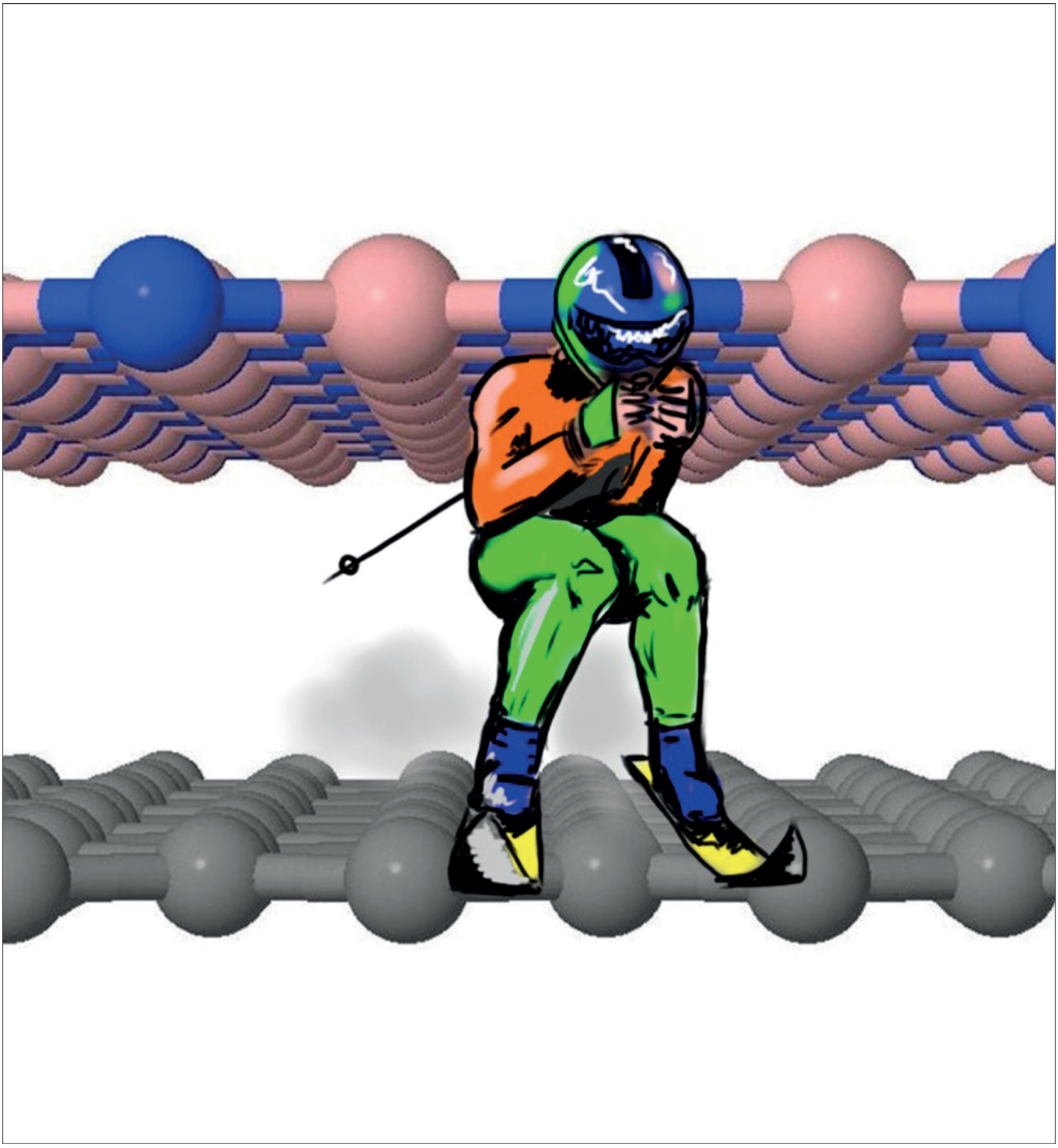

WILEY ONLINE LIBRARY © 2013 Wiley-VCH Verlag GmbH & Co. KGaA, Weinheim

Nanoscale tribology is an active and rapidly developing area of research that poses fundamental scientific questions that, if answered, may offer great technological potential in the fields of friction, wear, and lubrication. When considering nanoscale material's junctions, surface commensurability often plays a crucial rule in dictating the tribological properties of the interface. This Review surveys recent theoretical work in this area, with the aim of providing a quantitative measure of the crystal lattice commensurability at interfaces between rigid materials and relating it to the tribological properties of the junction. By considering a variety of hexagonal layered materials, including graphene, hexagonal boron nitride, and molybdenum disulfide, we show how a simple geometrical parameter, termed the "registry index" (RI), can capture the interlayer sliding energy landscape as calculated using advanced electronic structure methods. The predictive power of this method is further demonstrated by showing how the RI is able to fully reproduce the experimentally measured frictional behavior of a graphene nanoflake sliding over a graphite surface. It is shown that generalizations towards heterogeneous junctions and non-planar structures (e.g., nanotubes) provide a route for designing nanoscale systems with unique tribological properties, such as robust superlubricity. Future extension of this method towards nonparallel interfaces, bulk-material junctions, molecular surface diffusion barriers, and dynamic simulations are discussed.

1. Introduction

Tribology, the science of friction, wear, and lubrication, is of fundamental importance in many branches of pure and applied science. Understanding the physical processes that take place when two surfaces are brought into contact, separated, or displaced with respect to each other, has crucial implications on a wide range of research fields, including mechanics, electro-mechanics, and chemical catalysis, as well as on several subfields of biology. Over the past two decades, the science of tribology has faced new challenges, with the successful design and fabrication of microscopic and nanoscopic mechanical, electromechanical, and electronic components with unprecedented accuracy. Such components are expected to revolutionize many technological areas, thus leading not only to higher-capacity devices but also to the emergence of new functionalities, which rely on unique physical phenomena that appear at decreased dimensions and length scales. A major obstacle that limits the widespread use of miniature (electro)mechanical devices is their high surface-to-volume ratio, which leads to severe friction and wear, thus considerably decreasing their durability. The introduction of traditional liquid-phase lubricants often fails to decrease friction because they become too viscous when placed under such nanoscale constrictions.[1] This problem has led to the emergence of nanotribology,[1a,2] a new developing field that studies tribological effects that occur on the nanometer scale, where atomic forces play a crucial role in determining the final behavior of a system. In this respect, one of the primary goals of nanotribology is the design of new materials that present low friction on the atomic level. Not only are such materials expected to enhance the applicability of miniaturized devices, but they will also improve lubrication schemes at macroscopic interfaces.[3]

Two major challenges need to be addressed towards achieving this goal: First, a clear and deep understanding of tribological processes that occur on the atomic scale has to be gained. Once such understanding has been achieved, the next challenge is to relate the atomic-scale structure and dynamics of an interface to its tribological behavior over the full hierarchy of length scales, ranging from the nanoscale up to the macroscale. Overcoming these two challenges will enable the accurate design of new materials with desired tribological properties and functionalities.

During recent years, many experimental efforts have been directed towards gaining a clearer picture of friction on the atomic scale. Revolutionary techniques, such as friction force microscopy and spin-echo spectroscopy, have revealed important factors that govern friction and wear at dry nanoscale contacts.[4] Notably, surface incommensurability[4ak,au,bb,5] and induced vertical fluctuations[6] have been identified as key factors in achieving ultralow friction at nanointerfaces. Unlike the latter case, which requires external manipulation of the contacting bodies, surface incommensurability is often a naturally occurring interfacial property. Recent experiments on pristine layered materials have shown a strong dependence of the interlayer sliding friction on the misfit angle where friction was found to almost vanish when sliding occurred out of registry.[4a-k,au,5a,e–h,7] This unique phenomenon, termed superlubricity,[4a-k,5a–d,7,8] marks layered materials to serve as promising candidates as active components in nano-electromechanical systems (NEMS)[9] and as improved lubricants for macroscopic devices.[3]

Whilst such new experiments offer valuable information on nanoscale friction processes, the decreased dimensions and length scales that characterize nano-electromechanical systems offer a unique opportunity for the use of highly accurate computational tools to guide experimental efforts towards the design of materials with new functionalities. Numerous computational studies have addressed the origins of atomic-scale wear and friction in general and the occurrence of superlubricity in particular. Most of these studies use either phenomenological[4c,g–i,s,5d,j,m,n,6e,f,8,10] or atomistic[5d,10g,ac,al,11] representations of a small fraction of the relevant interface and solve Newton's equations of motion either numerically or through analytical analysis, which is based on effective Hamiltonians that are constructed to mimic the main inter-surface interactions that are responsible for friction and wear. Phenomenological simula-

[a] *Dr. O. Hod*
Department of Chemical Physics
School of Chemistry
The Raymond and Beverly Sackler Faculty of Exact Sciences
Tel-Aviv University, Tel-Aviv 69978 (Israel)
E-mail: odedhod@tau.ac.il

© 2013 Wiley-VCH Verlag GmbH & Co. KGaA, Weinheim

tions often rely on the so-called Prandtl–Tomlinson[10a,j] or Frenkel–Kontorova[12] models and their extensions, in which the friction that occurs during the relative motion of two bodies is modeled by the dynamics of particles that move on generic periodic potentials that represent the underlying surface whilst being subject to harmonic interactions. On the other hand, atomic simulations rely on empirical potentials that are constructed to fit structural and thermochemical molecular data that are either obtained experimentally or by using high-accuracy quantum-chemistry methods.

Both of these methods have been highly successful in interpreting experimental observations and in providing valuable insight into the atomic-scale processes that govern friction and wear.[13] Nevertheless, because they rely on effective Hamiltonians and classical mechanics, several issues may arise: 1) For atomistic simulations, the construction of reliable force fields is a non-trivial task that has to be performed separately for each system; 2) phenomenological models, in which the effective Hamiltonians are more robust, are designed to describe universal effects rather than the behavior of specific interfaces; 3) the $O(n)$–$O(n^2)$ scaling of molecular dynamics (MD) simulations with the number of particles, n, limits their ability to modeling relatively small NEMS devices; and 4) the degree of complexity of the simulations often makes it hard to identify and isolate the important physical parameters, which underlie the tribological processes that are being studied, on the atomic level.

Herein, we review recent work on the "registry index", which is a simple and intuitive tool for quantifying interfacial commensurability and for studying (with marginal computational effort) the tribological properties of rigid nanoscale material junctions. We start by illustrating the concept of the RI by using the case of a homogeneous graphene interface. In this example, we show how the RI can reproduce—down to fine details—experimental measurements of the friction of a graphene flake as it slides over a graphite surface. Next, we extend this model to the case of bilayer hexagonal boron nitride (*h*-BN) and to the more-challenging layered material molybdenum disulfide (2*H*-MoS_2), which serves as a representative example of the family of metal dichalcogenides that have an intricate sub-layer structure. We continue by considering the heterogeneous interface between graphene and *h*-BN, showing how it can sustain a robust superlubric state, owing to the natural mismatch between the lattice constants of the two materials. Finally, we show how this concept can be generalized to treat non-planar systems, such as double-walled boron-nitride nanotubes (DWBNNTs).

Oded Hod received his B.Sc. from the Hebrew University, Israel, in 1994 and his Ph.D. from Tel-Aviv University, Israel, in 2005. After completing a postdoctoral term at Rice University, USA, he joined Tel Aviv University in 2008. His research involves computational nanomaterials science including electronic structure, mechanical and electromechanical properties, density functional theory, molecular electronics, and electron dynamics in open quantum systems. Dr. Hod is a member of the Global Young Academy, the Israeli Young Academy, and the Lise-Meitner–Minerva Center for Computational Quantum Chemistry, and serves as the Israeli coordinator of the European Graphene Flagship Program and as the Head of the Israeli CECAM node. He received Tel-Aviv University's 2012 Rector's Award for Excellence in Teaching.

2. The Registry Index of Graphene

The RI is a numerical parameter that was designed to quantify the interfacial registry mismatch between two lattices. It is defined as a material-specific function that requires input regarding the surface lattice structures and the optimal and worst (in terms of total energy) inter-surface stacking modes. The general concept is best illustrated by the case of the homogeneous interface in bilayer graphene.[14] For this system, the worst stacking mode is the AA configuration, in which the lattices of the two layers are fully eclipsed (Figure 1 a), whilst the optimal stacking mode is the AB configuration, in which half of the carbon atoms in one layer reside atop the hexagonal centers of the adjacent layer (Figure 1 b). To define the RI, each atomic center is assigned a circle and the projected overlap between circles that belong to one layer and their counterparts on the adjacent layer is labeled by S_{CC} (Figure 1 c). Similar to the total energy, this overlap reaches a maximum value at the worst (AA) stacking mode and a minimum value at the optimal (AB)

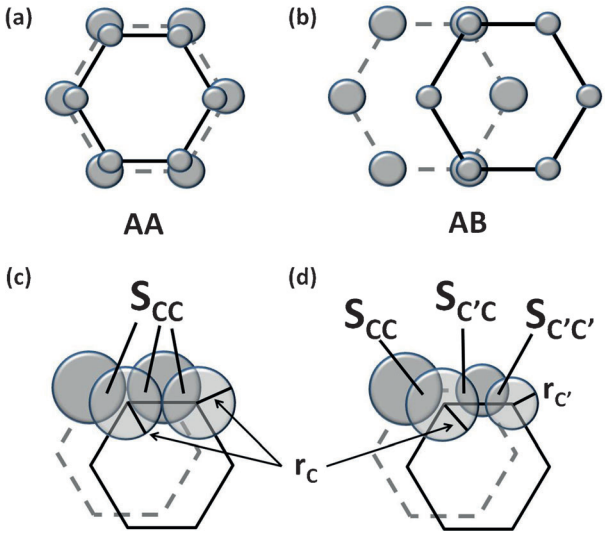

Figure 1. a) Worst (AA) stacking mode of a graphene bilayer. b) Optimal (AB) stacking mode of a graphene bilayer. c) Registry-index definition of the projected overlap area in bilayer graphene between circles that are assigned to atomic positions in the upper (transparent circles, solid lines) and lower layers (opaque circles, dashed lines). d) RI definition of the projected overlap area in multilayer graphene between circles that are assigned to atomic positions in the upper (transparent circles, solid lines) and lower layers (opaque circles, dashed lines). In panels (c) and (d), the circles that represent the carbon atoms are omitted for clarity. Figure reproduced with permission from ref. [14b].

© 2013 Wiley-VCH Verlag GmbH & Co. KGaA, Weinheim

interlayer configuration. Because we were looking for a numerical parameter that quantifies the interlayer registry in accordance with the relative total energies of different stacking modes, we chose the RI to be proportional to the total overlap area, that is, $RI \propto S_{CC}$. Normalizing this expression to the overlap values at the worst (S_{CC}^{AA}) and optimal (S_{CC}^{AB}) stacking modes, according to Equation (1), affords a parameter that is bound to the range [0,1], where RI = 1 at the worst stacking mode and RI = 0 at the optimal configuration.

$$RI_{graphene} = \frac{S_{CC} - S_{CC}^{AB}}{S_{CC}^{AA} - S_{CC}^{AB}} \quad (1)$$

Just one fitting parameter remains to be set, which is the radius of the circles that are associated with the carbon atoms. The fitting procedure for this parameter is performed once per material. This is done by plotting the RI for various relative lateral interlayer shifts parallel to the basal planes of the bilayer graphene system and finding the optimal circle radius that produces the best-fit to the sliding-energy landscapes, obtained from higher-level calculations for the smallest possible unit cell. When comparing the obtained RI landscape (Figure 2)

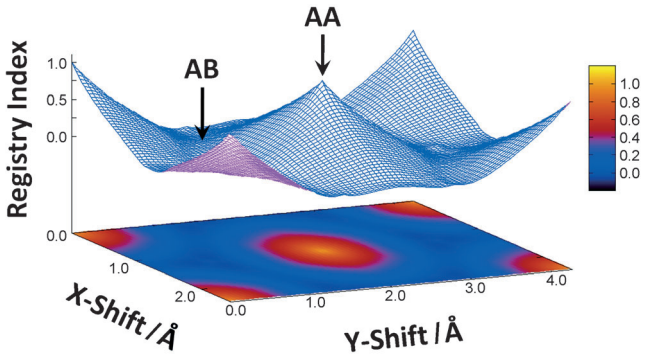

Figure 2. RI landscape for interlayer sliding in bilayer graphene. The location of the AA and AB stacking modes are indicated by black arrows. Figure reproduced with permission from ref. [14a].

to molecular dynamics[15] and dispersion-augmented tight-binding[16] calculations of the sliding-energy landscape of graphene, it is clear that, with a circle radius of $r_C = 0.5\ L_{CC}$ (where $L_{CC} = 1.42$ Å is the covalent carbon–carbon bond length in graphene), the RI model captures all of the important physical characteristics of the sliding potential of this system.[14a]

One may wonder how such a simple geometrical parameter is capable of accurately capturing the complex sliding-energy landscape of the layered interface. To explain this fact, we recall that the major contribution to the sliding corrugation comes from variations in the repulsion between overlapping electron clouds of atoms that belong to the two adjacent layers as they cross each other during the sliding process. These interactions, which are often associated with Pauli repulsions, are short range in nature and, thus, it is sufficient to consider overlap between electron clouds that are associated with neighboring atomic sites of the two layers. Hence, two important factors are required to describe the sliding-energy landscape: 1) The extent of the atomic electron clouds and 2) the degree of their local overlap. In the RI formulation, the former factor is modeled by the atom-centered circle radii, whereas the latter is depicted by the calculated circle overlaps.

3. Superlubricity of Graphite from the Viewpoint of the Registry Index

Once the RI has been defined for a given material, it can be used to analyze and guide experimental efforts towards controlling the friction in NEMS devices that are constructed from this material. This is especially true for the study of superlubricity, for which a direct relationship between the registry mismatch and the measured friction between two rigid layers has been postulated.[5b–d] To demonstrate this relationship, we will consider recent experimental results that have provided clear evidence for the occurrence of superlubricity in graphite.[5a,7] Here, the friction between a graphene flake and a graphitic surface was measured as a function of the misfit angle. When the two lattices were commensurate, measurable friction occurred, whereas, for incommensurate configurations, practically frictionless motion was obtained (Figure 3c).

To model this phenomenon by using the RI, we will consider the system shown in Figure 4, in which a finite rigid hexagonal flake slides atop an infinite rigid graphene surface.[14b] Two important parameters are used to characterize this sliding scenario: 1) The misfit angle and 2) the sliding direction. The misfit angle is the angle at which the flake is rotated about an axis that crosses its center of mass (perpendicular to its basal plane), such that 0° represents the orientation of the flake in the AB staking mode, and the latter parameter is the direction along which the flake is dragged with respect to the armchair axis of the underlying hexagonal graphene layer. By calculating the RI at various misfit angles along different sliding directions, we can map the sliding-energy landscape of the hexagonal flake. Figure 3a shows RI profiles for several misfit angles that were calculated at a sliding direction parallel to the armchair axis of the underlying graphene layer. For the commensurate case (misfit angles of 0° and 60°), in which the sliding path crosses both the optimal and the worst stacking modes of the bilayer system, the RI profile shows large variations that span the full range of allowed RI values. Interestingly, for the incommensurate configuration, a qualitatively different behavior is obtained, in which relatively small variations occur around an average RI value of about 0.2 as the flake is dragged along the linear path. Because the RI landscape mimics well the variations in total sliding energy, we may interpret these results such that, for commensurate interlayer configurations, relatively high sliding-energy barriers are obtained, whereas, for incommensurate geometries, the overall roughness of the sliding-energy curve is small. Noting that, for a dry, rigid interface, both static and dynamic friction are related to the corrugation of the sliding-energy landscape, we plot the amplitude of the RI variations along a given path as a function of the misfit angle and compare the results to the measured friction. In Figure 3c, the RI results are presented along with the experimen-

© 2013 Wiley-VCH Verlag GmbH & Co. KGaA, Weinheim

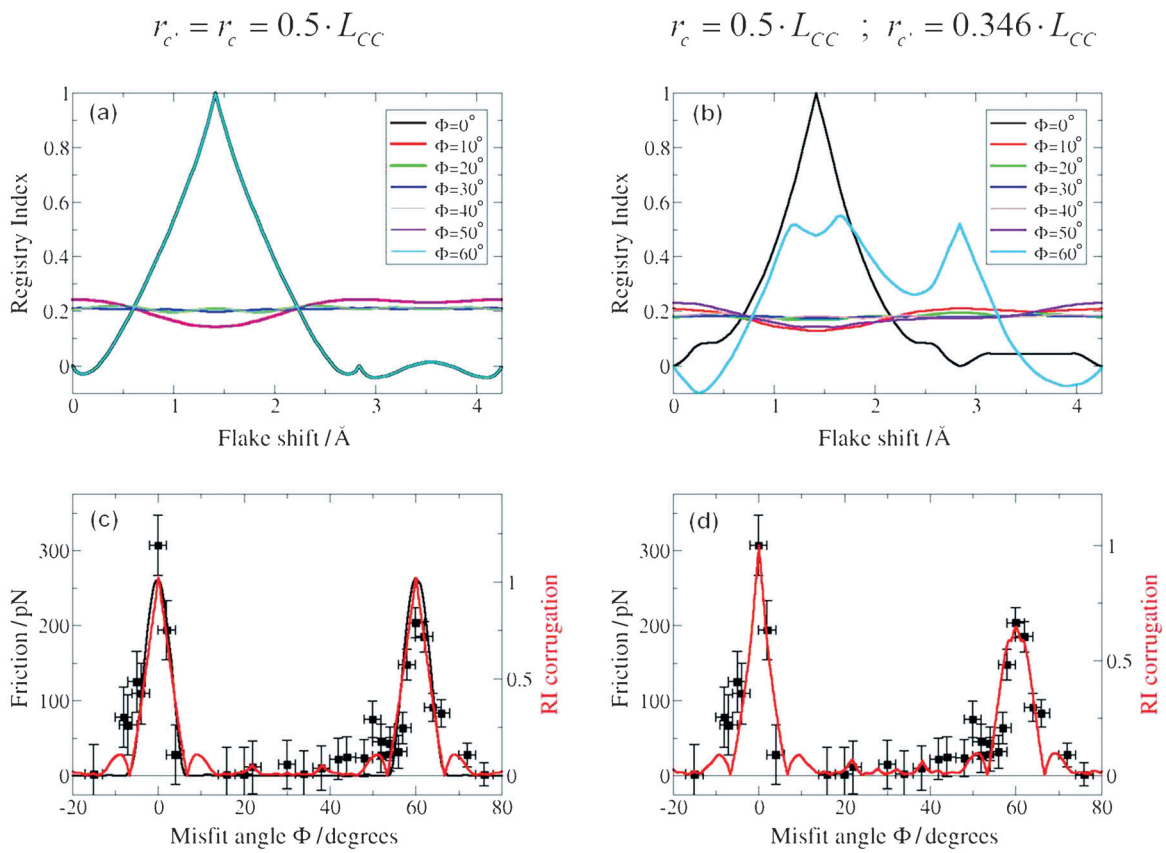

Figure 3. Dependence of the RI on the misfit angle (Φ) of a 150-atom hexagonal graphene flake: a, b) Variation in the RI along linear sliding paths at different misfit angles for a single graphene flake on a single graphene sheet (a) and for a multilayer graphene flake on the graphite surface (b). c, d) Plots of measured friction (black circles, left axis) and corrugation of the RI landscape along linear paths (red line, right axis) as a function of the misfit angle for the bilayer (c) and multilayer systems (d). The sliding direction was chosen to be along the armchair axis of the infinite graphene layer, as shown in Figure 1 a. Experimental results are reproduced with the kind permission and help of Prof. Joost W. M. Frenken and Prof. Martin Dienwiebel from ref. [5]. Diagram reproduced with permission from ref. [14b].

tally measured friction, showing that the RI model provides an excellent description of the tribological properties of this system.

The RI model can be further fine-tuned to capture some delicate details of the frictional behavior at the graphitic interface. To demonstrate this fact, we notice that, despite the expected six-fold symmetry, the measured frictions at 0° and 60° are different. This result has been attributed to the fact that, experimentally, both the surface and the flake have a multilayer structure that is assumed to possess an ABA stacking mode.[8b] Hence, each couple of neighboring carbon sites (marked as C and C′) become inequivalent, with one site residing atop a carbon atom and the other site atop the center of a hexagon of the adjacent layer (Figure 1 b). This inequivalence results in slightly different shapes and sizes of the π-electron clouds near the C and C′ sites, thereby leading to somewhat altered Pauli repulsions between them as different sites that belong to the flake and the infinite surface pass over each other during the sliding process. Therefore, the six-fold symmetry reduces to a three-fold symmetry and the high friction peaks at 0° and 60° become asymmetric. In the RI approach, this can easily be modeled by assigning different circle radii, which represent the relative sizes of the electron clouds near the C and C′ atomic centers (Figure 1 d). Figure 3 b is the equivalent of Figure 3 a, with circle radii of $r_C = 0.5\ L_{CC}$ and $r_{C'} = 0.346\ L_{CC}$. Upon breaking the symmetry between the C and C′ sites, the RI variations at $\Phi = 0°$ and $\Phi = 60°$ are no longer equivalent and the overall corrugation in the latter case is smaller. For intermediate angles, minor difference between the multilayer and bilayer representations are obtained, with very similar average corrugation and deviations in both cases. By plotting the amplitude of these variations as a function of the misfit angle, Figure 3 d represents the equivalent of Figure 3 c for a multilayer case, where the peak asymmetry is now fully captured. The remarkable agreement between the experimentally measured friction and the calculated RI results, both in the high- and low-friction regimes, again demonstrates that the RI model can be used as a simple, intuitive, and computationally efficient tool for predicting the tribological properties of nanoscale interfaces in rigid layered materials.

Here, it should be emphasized that the RI concept is designed to capture structural effects that, as discussed above, can lead to variations of two orders of magnitude in the measured friction of the system. Energy-dissipation channels, such as the phonons' degrees of freedom and the formation of electron/hole pairs during the sliding process, are not taken into

© 2013 Wiley-VCH Verlag GmbH & Co. KGaA, Weinheim

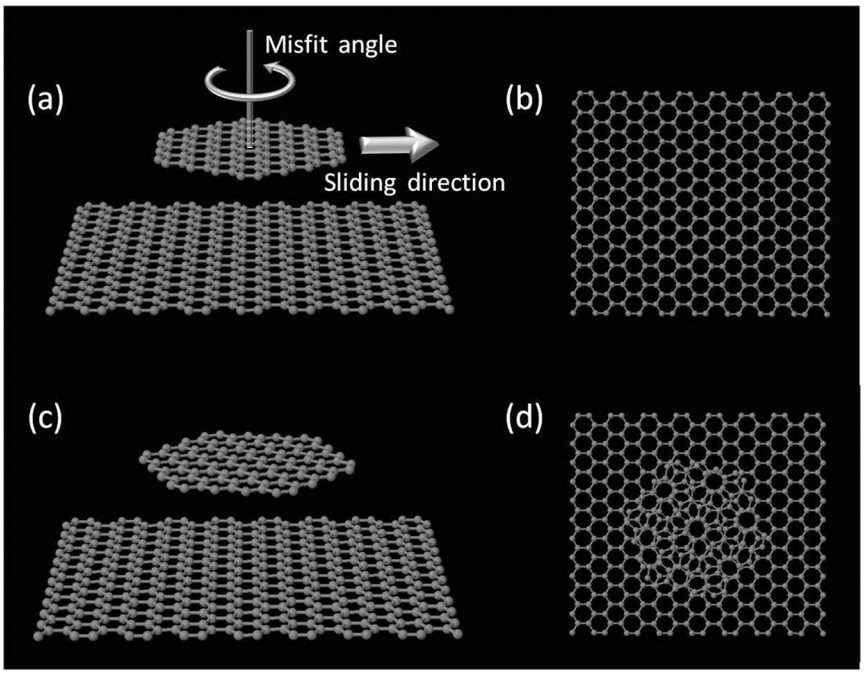

Figure 4. Commensurate (a, b) and incommensurate (c, d) configurations of a graphene flake atop a graphene surface. The definitions of the sliding direction and the misfit angle are indicated in (a). The misfit angles for the presented commensurate and incommensurate modes are 0° and 20°, respectively. Clear Moiré patterns for the incommensurate state appear in panel (d). Figure reproduced with permission from ref. [14b].

account in the explicit formulation of the model. Nevertheless, when considering the wear-less dynamics of rigid nanoscale materials interfaces, structural effects often dominate their tribological properties, thus making the RI concept applicable to a wide range of scientifically intriguing and technologically relevant systems.

4. The Registry Index of Hexagonal Boron Nitride

The hexagonal phase of boron nitride can be viewed as the inorganic counterpart of graphite. Both materials share the same intra-layer structure, in which the two carbon atoms in the hexagonal unit cell of graphene are replaced by a boron-nitride pair in *h*-BN. Both materials are isoelectronic; nevertheless, the electronegativity differences between the boron and nitrogen atoms results in a polar covalent bond, which dictates different optimal and worst interlayer stacking modes. Here, the AA′ configuration, in which a partially positively charged boron atom of one layer resides atop a partially negatively charged nitrogen atom of its adjacent layer, is the optimal stacking mode, whereas the AA configuration, in which both layers are fully eclipsed, is the worst (Figure 5b).

Because the interlayer-sliding physics is determined by the repulsion between overlapping electron clouds, which have different shapes and sizes in the two materials, one could expect that the sliding-energy landscape of the two interfaces would also differ, thus resulting in altered tribological properties. To check the validity of these assertions, the RI model should be extended to treat the homogeneous interface of bilayer *h*-BN.[14b,17] A similar procedure to that used to define the RI of graphene is employed, in which each atomic center is assigned a circle. The projected overlaps between circles that belong to atomic sites of the two layers are summed appropriately to produce the RI of *h*-BN, which is normalized to obtain a value of $RI_{h\text{-}BN}=0$ at the optimal (AA′) stacking mode and $RI_{h\text{-}BN}=1$ at the worst (AA) stacking mode, according to Equation (2), where S_{NN} (S_{BB}) is the projected overlap between circles that belong to nitrogen (boron) atoms on two adjacent layers at an arbitrary stacking mode and S_{NB} is the projected overlap between a nitrogen circle on one layer and a boron circle on the other (Figure 5c). $S_{NN}^{AA'}$, $S_{BB}^{AA'}$, $S_{NE}^{AA'}$, S_{NN}^{AA}, S_{BB}^{AA}, and S_{NB}^{AA} are the values of these overlaps at the AA′ and AA stacking modes, respectively.

$$RI_{h-BN}=\frac{\left(S_{NN}-S_{NN}^{AA'}\right)+\left(S_{BB}-S_{BB}^{AA'}\right)-\left(S_{NB}-S_{NB}^{AA'}\right)}{\left(S_{NN}^{AA}-S_{NN}^{AA'}\right)+\left(S_{BB}^{AA}-S_{BB}^{AA'}\right)-\left(S_{NB}^{AA}-S_{NB}^{AA'}\right)} \quad (2)$$

Because the electron cloud around the nitrogen atom in *h*-BN is more delocalized than that around the boron atom,[18] the radius of the circle that is assigned to nitrogen atomic sites is taken to be larger than its boron counterpart ($r_N > r_B$). The ratio between the two radii is adjusted to produce good agreement between the calculated sliding RI surfaces for the infinite bilayer *h*-BN system and the corresponding sliding-energy landscapes, as obtained by using advanced density functional theory (DFT) calculations. Figure 5a, d shows a comparison between the sliding-energy landscape of bilayer *h*-BN, as calculated by using the Tkatchenko–Scheffler–van der Waals (TS–vdW) dispersion-augmented PBE[19] exchange-correlation density functional approximation,[17,20] and the corresponding sliding RI surface, as obtained with $r_N = 0.5\ L_{BN}$, $r_B = 0.15\ L_{BN}$, and $L_{BN} = 1.45$ Å (the boron–nitride covalent distance in *h*-BN). Similar to the case of bilayer graphene, all of the important physical features that appear in the sliding-energy landscape of *h*-BN are appropriately captured by the RI model, with marginal computational effort.

With the definition of the RI of *h*-BN in hand, we can now explore the occurrence of superlubricity at the homogeneous *h*-BN interface. To this end, we follow the same procedure as described above for a graphene flake sliding atop a graphene surface. The setup is identical to that shown in Figure 4, with both the graphene flake and the underlying graphene surface replaced by their *h*-BN counterparts. The flake is then rotated

© 2013 Wiley-VCH Verlag GmbH & Co. KGaA, Weinheim

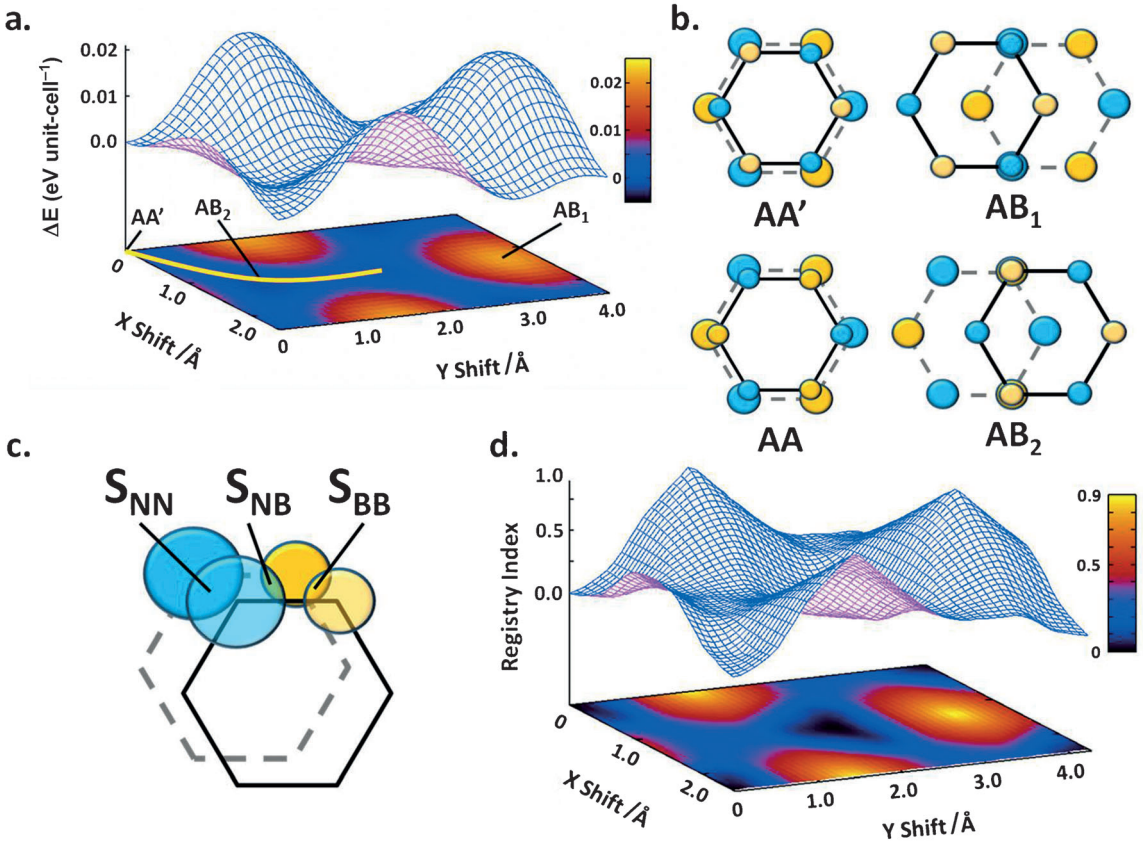

Figure 5. Definition of the RI of *h*-BN: a) Sliding-energy landscape of bilayer *h*-BN, as calculated by using the TS–vdW dispersion-corrected PBE exchange–correlation density functional approximation. b) Definition of some high-symmetry stacking modes of bilayer *h*-BN. c) Definition of the circle overlaps that are used in the RI expression. d) Sliding RI surface of bilayer *h*-BN. Blue (yellow) circles represent nitrogen (boron) atomic sites. Figure reproduced with permission from ref. [17].

and shifted along the underlying surface in various sliding directions and the RI corrugation (maximum amplitude of the RI variations) along each linear path is plotted as a function of the misfit angle and sliding direction. Figure 6 shows the dependence of the RI corrugation on the size of the hexagonal flake and the sliding direction. A very similar pattern to that obtained for bilayer graphene (Figure 3a, c) is obtained, that is, high friction is expected to be measured at 0° and 60°, whilst superlubric behavior should occur at intermediate angles (Figure 6a). Despite the fact that the nitrogen and boron circles are different, when sliding along the armchair axis of the infinite *h*-BN layer, the two peaks are almost identical. This result is due to the different definition of the RI, which stems from the different optimal and worst stacking modes of graphene and *h*-BN. When considering other pulling directions, the peak symmetry breaks and a very similar picture to that obtained for the multilayer graphene system is obtained (Figure 6b).

5. The Registry Index of Molybdenum Disulfide

Having established the suitability of the RI concept for describing the sliding-energy landscape of simple layered materials, an intriguing question arises, that is, can this method be further extended to treat more-complex layered compounds? With this question in mind, a natural testing ground would be the family of metal dichalcogenides, which, along with the interlayer stacking, also possess a complex intra-layer structure. Thus, next, we consider a prominent member of this family, namely the hexagonal phase of molybdenum disulfide (2*H*-MoS_2), which is known to serve as an excellent solid lubricant.[4ak,11g,h] Similar to graphene and *h*-BN, the 2*H*-MoS_2 crystal has a layered structure in which the individual layers have hexagonal lattice symmetry. Nevertheless, in the latter case, each layer consists of three sub-layers that are organized such that a molybdenum sheet is sandwiched between two sulfur sub-layers (Figure 7).

To define the RI of MoS_2, a similar procedure to that employed for flat layered materials is used, in which circles are assigned to the various atomic positions within each layer.[21] We recall that, in our simplistic treatment, when two atoms that reside on adjacent layers are positioned directly atop each other, their circular overlap represents the degree of overlap between their associated electron clouds. Therefore, the assigned radii should reflect the relative distances between the different atomic positions in the two layers. Hence, unlike the case of flat layered materials, in this case, we need to ascribe to each atomic position three circles, which represent the different interlayer interactions between the various sub-layers. These radii are denoted as r_α^β, where α is the atom around

© 2013 Wiley-VCH Verlag GmbH & Co. KGaA, Weinheim

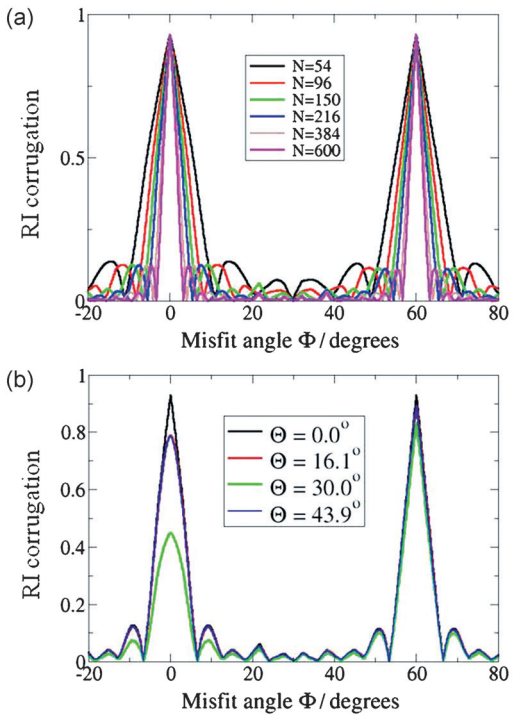

Figure 6. Dependence of the RI peak shape on the *h*-BN flake size and the sliding direction: a) Plot of the RI corrugation as a function of the misfit angle for several flake sizes in the bilayer system; *N* represents the number of atoms in the flake. b) Plot of the RI corrugation as a function of the misfit angle for various sliding directions in the bilayer *h*-BN system. Figure reproduced with permission from ref. [14b].

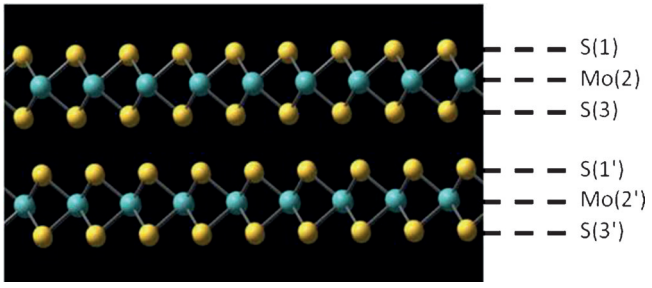

Figure 7. Two MoS_2 layers at the optimal (AA′) stacking mode, thus emphasizing their sub-layer structure. Figure reproduced with permission from ref. [21].

which the circle is centered and β is the corresponding atom on the other layer (Figure 8a, b). In practice, it is sufficient to only consider the interactions between the inner sub-layers (namely, 1′-3, 1′-2, and 2′-3 in Figure 7) and, to obtain an optimal fit with DFT calculations (Figure 9, bottom), the corresponding radii are chosen as follows: $r_S^S = 0.9$ Å, $r_S^{Mo} = 0.8$ Å, and $r_{Mo}^S = 0.3$ Å.

Next, the optimal and worst (in terms of total energy) interlayer stacking modes have to be identified. The optimal (most energetically stable) interlayer configuration is known to be the AA′ stacking mode, in which sulfur atoms of one layer reside atop molybdenum atoms of the other layer (Figure 8c).[5i] Starting from this configuration, the worst (highest in energy) laterally shifted interlayer configuration is the AB_2

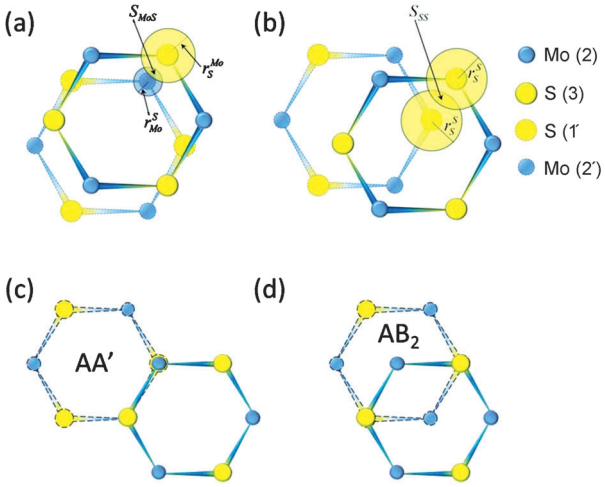

Figure 8. Projected circle overlaps (a, b) and high-symmetry stacking modes (c, d) in a 2*H*-MoS_2 bilayer. Figure reproduced with permission from ref. [21].

stacking mode, in which the positions of sulfur atoms from both layers are fully eclipsed and the molybdenum atoms reside above the centers of the hexagons in the adjacent layers (Figure 8d). We note that the Mo/S overlap (S_{MoS}, Figure 8a) is a maximum in the optimal stacking mode, whereas the S/S overlap (S_{SS}, Figure 8b) is maximum in the worst stacking mode. By setting $RI \propto (S_{SS} - S_{MoS})$, we obtain a parameter that is minimal at the optimal stacking mode and maximal at the worst stacking mode, as desired. Finally, normalizing this expression to the range [0:1] yields Equation (3), where $S_{SS}^{AA'}$ and $S_{MoS}^{AA'}$ are the S/S and Mo/S overlaps at the AA′ stacking mode, respectively, and $S_{SS}^{AB_2}$ and $S_{MoS}^{AB_2}$ are the S/S and Mo/S overlaps at the AB_2 stacking mode, respectively.

$$RI_{2H-MoS_2} = \frac{\left(S_{SS} - S_{SS}^{AA'}\right) - \left(S_{MoS} - S_{MoS}^{AA'}\right)}{\left(S_{SS}^{AB_2} - S_{SS}^{AA'}\right) - \left(S_{MoS}^{AB_2} - S_{MoS}^{AA'}\right)} \quad (3)$$

With the definition of the RI for 2*H*-MoS_2 in hand, we can now compare the sliding-energy landscape that is obtained from DFT calculations to the predictions of the RI model. As shown in Figure 9a, the sliding RI surface, as obtained by using the circle radii given above, is able to capture all of the important physical features that appear in the calculated sliding-energy landscape under an external pressure of 500 MPa at the local density approximation level of theory.[5i] To emphasize the agreement between the two calculations in Figure 9c, d, we present slices of the full RI and the sliding-energy landscape, respectively, along specific pathways that pass through the different surface minima and maxima. Here as well, remarkable agreement between the RI variations and the DFT energy variations is also obtained.

The general nature of the RI model can be further exemplified by considering the results of recent DFT calculations of the sliding-energy landscape of 2*H*-MoS_2 under a considerably higher external pressure of 15 GPa.[22] Under these conditions, the repulsions between electron clouds of atoms that belong to two adjacent layers are considerably enhanced and the sym-

© 2013 Wiley-VCH Verlag GmbH & Co. KGaA, Weinheim

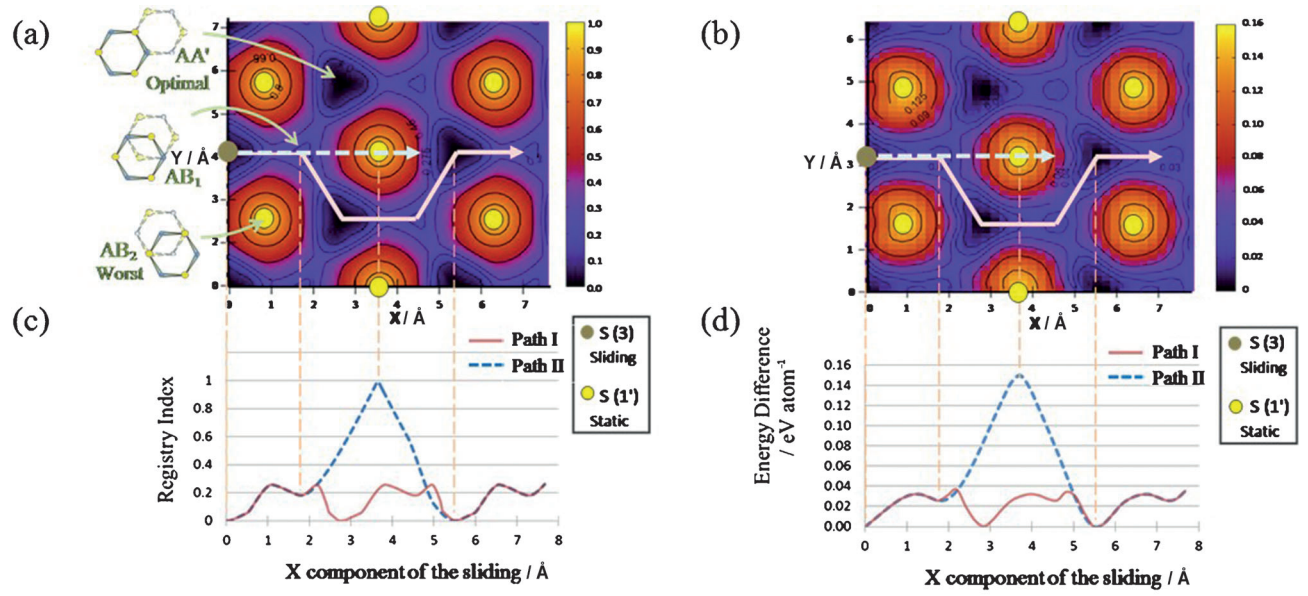

Figure 9. Interlayer-sliding-energy landscape of bilayer 2*H*-MoS_2. Top: Variations in the RI (a) and total DFT energy [eVatom^{-1}] (b), as a function of lateral interlayer displacement. Bottom: Variations in the RI (c) and total DFT energy (d) along specific sliding pathways as denoted in (a) and (b), respectively. The DFT results, under an external pressure of 500 MPa, were reproduced with the kind permission and help of Prof. Simon R. Phillpot and co-workers from ref. [5i]. Figure reproduced with permission from ref. [21].

metry in the sliding-energy landscape increases (Figure 10b). By making an appropriate choice of the circle radii, the RI landscape can be tuned to reproduce the results of the higher-pressure DFT calculations (Figure 10a).

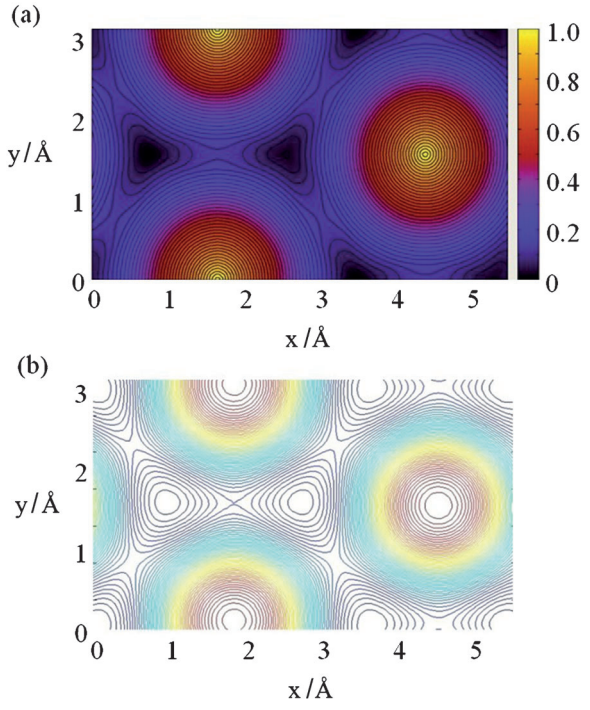

Figure 10. 2*H*-MoS_2 interlayer RI surface (a) that was tuned to match the DFT sliding-energy landscape calculated at an external pressure of 15 GPa (b). The overall corrugation of the DFT sliding-energy landscape was about 1 eV. The DFT results are reproduced with the kind permission and help of Prof. S. Ciraci and co-workers from ref. [22]. Figure reproduced with permission from ref. [21].

Finally, a comparison of the radii of the different atomic circles that are used to reproduce the two DFT calculations may provide insight into the origin of the effects of external pressure on the overall sliding-energy landscape. Specifically, to produce the landscape shown in Figure 10b, r_S^S was kept at 0.9 Å and the other radii were shortened to $r_S^{Mo} = 0.15$ Å and $r_{Mo}^S = 0.1$ Å. This result indicates that, upon increasing the external load, the strong repulsions between the overlapping electron clouds of neighboring frontier sulfur atoms on the adjacent layers become the dominant factor in determining the sliding-energy landscape, whereas the interactions between the more-remote S-Mo sub-layers become relatively less important. This result further explains the increased symmetry in the sliding-energy landscape at higher external pressures.

6. Robust Superlubricity at the Heterogeneous Graphene/*h*-BN Interface

Apart from being an intriguing physical phenomenon, the occurrence of superlubricity in homogeneous layered systems, such as those discussed above, is expected to pave the road towards the design of materials interfaces with unique tribological properties. An interesting suggestion for a macroscopic ultralow-friction junction, in which finite graphene flakes that were dispersed between two multi-domain graphene surfaces with random orientations were shown to induce a global low-friction sliding state, was recently put forward.[23] Whilst this design shows great technological promise, achieving a stable superlubric behavior in homogeneous layered interfaces, such as those discussed above, is generally non-trivial. This is mainly due to dynamic effects, often associated with lattice reorientations, which have been shown to result in a considerable increase in the sliding friction.[4s,10r] A possible solution to this

© 2013 Wiley-VCH Verlag GmbH & Co. KGaA, Weinheim

problem was recently suggested that involved the introduction of heterogeneous material junctions, in which a naturally occurring lattice mismatch between the two crystals may result in low corrugation of the sliding-energy landscape, regardless of their relative orientation.[24]

One such layered structure, that has recently gained much interest, owing to its promising electronic properties, is the heterogeneous junction between graphene and *h*-BN.[25] In this case, the two lattices, which share the same intra-layer hexagonal structure, have a small lattice mismatch of about 1.8%.[25a,b,h–j] For sufficiently large graphene flakes that slide over a *h*-BN surface, this mismatch can induce a robust superlubric state that is independent of the interlayer misfit angle.

To demonstrate this property, one can define the RI for the heterogeneous interface. To this end, a strained unit cell of the bilayer structure is considered, in which the lattice vectors of the graphene and *h*-BN layers are taken to be identical. Under these constraints, the optimal stacking mode is obtained when one carbon atom in the graphene unit cell resides atop a boron atom in the *h*-BN unit cell and the other carbon atom resides atop the center of a *h*-BN hexagon.[25a,h] When the two lattices are completely eclipsed, the interlayer repulsions between overlapping electron clouds reach a maximum and the worst stacking mode is achieved.[25a,h]

When assigning circles to the various atomic position along adjacent lattices, two types of overlap occur (Figure 11): 1) S_{CN}, which is the projected overlap between circles that are assigned to a nitrogen atom in the *h*-BN layer and circles that are associated with the carbon atoms of the graphene layer; and 2) S_{CB}, which is the projected overlap between circles that are assigned to a boron atom in the *h*-BN layer and circles that are associated with the carbon atoms of the graphene layer. Because S_{CB} is maximal and S_{CN} is minimal at the optimal stacking mode and both overlaps obtain a maximum value in the worst stacking mode, the RI is taken to be proportional to the sum of both overlaps, that is, $RI \propto S_{CB}+S_{CN}$. Based on this definition, RI obtains a minimum value in the optimal stacking mode and a maximum value in the worst staking mode, as required. Next, as before, the RI is normalized to the range [0:1], according to Equation (4), where the value of 0 (1) is obtained in the optimal (worst) stacking mode. Here, S^A_{CB}, and S^A_{CN} are the carbon/boron and carbon/nitrogen projected overlap areas at the worst stacking mode and S^C_{CB}, and S^C_{CN} are the corresponding projected overlap areas at the optimal stacking mode.

$$RI_{graphene/h-BN} = \frac{(S_{CB} - S^C_{CB}) + (S_{CN} - S^C_{CN})}{(S^A_{CB} - S^C_{CB}) + (S^A_{CN} - S^C_{CN})} \quad (4)$$

Finally, the circles' radii are calibrated to obtain good agreement between the sliding RI surface and the sliding-energy landscape that was obtained from advanced DFT calculations. Figure 12b shows the calculated RI surface for different interlayer positions of the heterojunction, with $r_C = 0.5\ L_{CC}$, $r_N = 0.4\ L_{BN}$, $r_B = 0.2\ L_{BN}$ (Figure 11d), where the CC (L_{CC}) and BN (L_{BN}) bond lengths are taken to be equal ($L_{CC} = L_{BN} = 1.431$ Å) for the strained unit cell. The corresponding sliding-energy landscape, which was obtained by using the screened-exchange hybrid

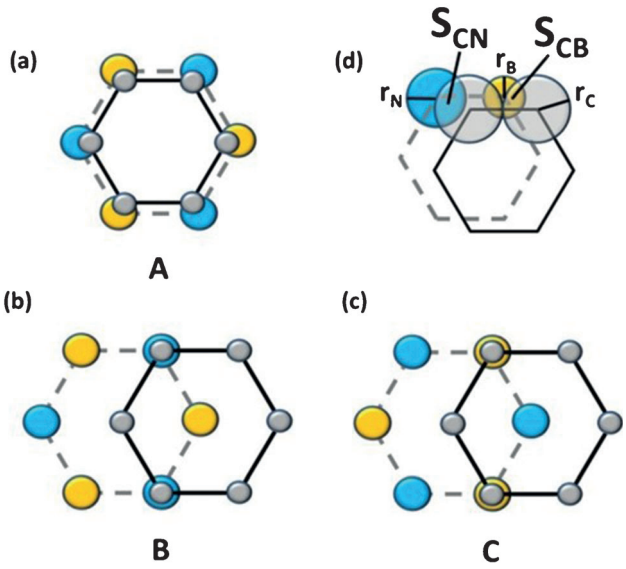

Figure 11. Representation of the high-symmetry stacking modes of graphene on *h*-BN: a) Worst (A) stacking mode, in which the graphene and *h*-BN layers are fully eclipsed. b) B stacking mode, in which half of the carbon atoms are atop nitrogen atoms and the rest are above hexagon centers of the *h*-BN hexagonal lattice. c) Optimal (C) stacking mode, in which half of the carbon atoms are atop boron atoms and the rest are above hexagon centers of the *h*-BN hexagonal lattice. d) Definition of the projected overlap areas that were used in the RI calculations. As schematically depicted, we chose $r_C > r_N > r_B$. Gray, yellow, and blue circles represent carbon, boron, and nitrogen atoms, respectively. Figure reproduced with permission from ref. [24].

HSE density functional approximation[26] with the double-ζ polarized 6-31G* Gaussian basis set,[27] as implemented in the Gaussian suite of programs,[28] is shown in Figure 12b. The agreement between the sliding-energy landscape, as calculated from first principles, and the sliding RI surface suggests that, even for the heterojunction, the RI model successfully captures the essential physical parameters that are required to describe the sliding-energy landscape. Furthermore, a simple scaling factor (of 28.2 meV/unit cell in this case) may be used to relate the results of the RI calculations to the sliding energies obtained using advanced DFT methods for such systems.

Once a consistent definition of the RI is obtained for the strained unit cell, it is possible to characterize the dependence of the sliding-energy corrugation on the misfit angle between the two mismatched lattices. For this purpose, we consider several finite rectangular graphene flakes that slide atop a *h*-BN layer with various interlayer orientations (Figure 13a). In equivalence with Figure 3 and Figure 6 for the homogeneous graphene and *h*-BN interfaces, respectively, Figure 13b shows the amplitude of the RI variations along linear sliding paths as a function of the misfit angle between the lattices of the graphene flake and the *h*-BN layer. For the smallest flake that is considered (5×5 graphene unit cells), a very similar picture to that obtained for the graphitic junction (Figure 3) is obtained, in which, at small misfit angles, the corrugation is high, decreasing as the misfit angle increases, and increasing again at about $\Phi = 60^\circ$, owing to the six-fold symmetry of the hexago-

© 2013 Wiley-VCH Verlag GmbH & Co. KGaA, Weinheim

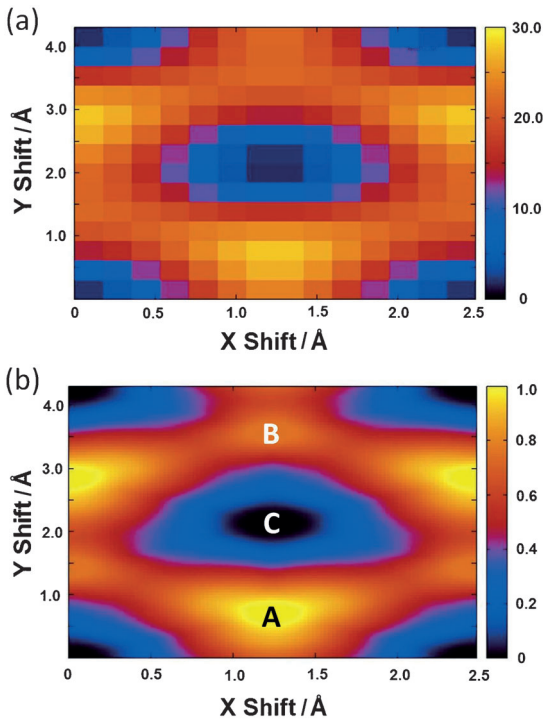

Figure 12. Interlayer-sliding energy (a) and RI landscapes (b) for graphene on *h*-BN, as calculated for the strained unit cell. Total energy differences in (a), in meV/unit cell, were calculated by using DFT at the HSE/6-31G* level of theory and a fixed interlayer distance of 3.3 Å. Capital letters in (b) mark the location of the high-symmetry stacking modes shown in Figure 11. Figure reproduced with permission from ref. [24].

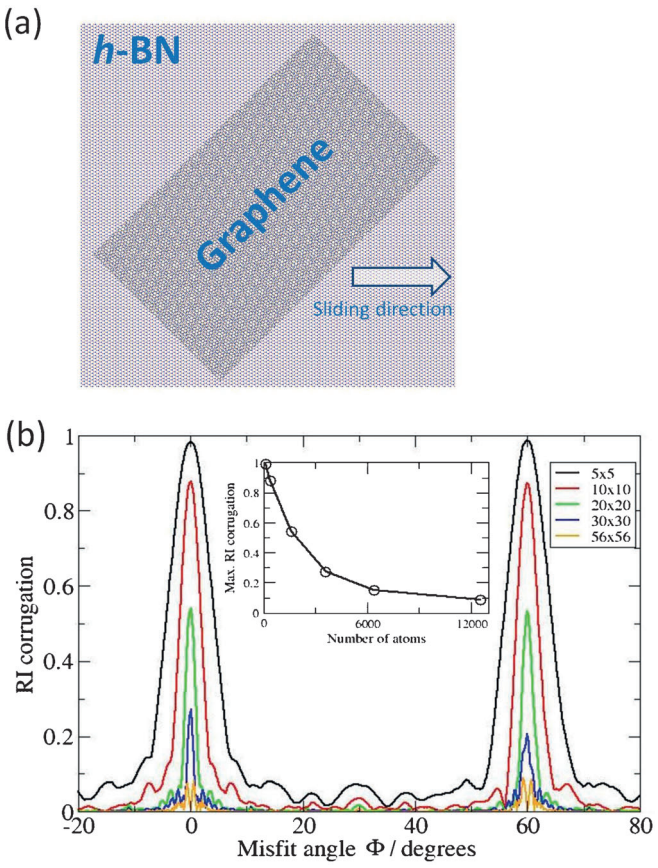

Figure 13. Effect of flake size and misfit angle on the corrugation of the sliding RI surface of the heterogeneous graphene/*h*-BN interface: a) Schematic representation of a rectangular 56×56 unit cells graphene flake sliding on top of a *h*-BN layer with a misfit angle of 45°. The sliding direction is indicated by a white arrow. b) Plot of maximum variations in the RI, as calculated for linear paths along the sliding direction, as a function of interlayer misfit angle. Inset: Plot of maximum RI corrugation as a function of flake size (number of atoms in the flake). The diagrams in (b) are normalized to the size of the relevant graphene flake, such that a maximum RI corrugation of 1 is obtained for a strained graphene flake that consists of the same number of atoms and geometry with no lattice mismatch with the underlying *h*-BN layer. Figure reproduced with permission from ref. [24].

nal lattice. As the size of the flake increases, the overall RI corrugation decreases monotonously: For a graphene flake the size of 56×56 unit cells, the maximum obtained RI corrugation is less than 10% of that calculated for a strained flake (with no graphene/h-BN lattice mismatch) of same dimensions (Figure 13b, inset). By using the scaling relationship obtained above for the strained unit cell, one can estimate the maximal sliding-energy corrugation for this flake to be about 0.62 meV/atom. It should be emphasized that even this value is limited to a very narrow region of misfit angles beyond which the sliding RI corrugation becomes negligible for any practical purpose. This result indicates that graphene flakes of appropriate dimensions that slide atop a *h*-BN layer should exhibit a vanishingly small sliding friction, regardless of the relative orientation between the two lattices, thus resulting in a stable and robust superlubric state.

7. Beyond Planar Structures: Boron-Nitride Nanotubes

In the discussion thus far, the RI concept has been shown to successfully describe the sliding-energy physics and related tribological properties of planar layered materials. Such systems often possess a compact unit cell, which can be readily treated by using advanced computational methods. Nevertheless, nano-electromechanical systems often involve more-complex structures, such as single and multi-walled nanotubes, which, apart from the simplest cases, are beyond the reach of state-of-the-art electronic structure methods. Therefore, to be able to provide an efficient and reliable treatment of the sliding physics of such systems, it is desirable to generalize the RI method to characterize systems that possess a finite curvature.

To demonstrate the generalization logic, we consider the case of double-walled boron-nitride nanotubes (DWBNNTs), for which an RI definition of the planar bilayer *h*-BN counterpart has already been established.[14a,17] The procedure to define the RI for this system is presented in Figure 14: First, the two nanotube walls are unrolled to form planar ribbons of different widths. Then, the narrower ribbon (the unrolled inner tube) is stretched to match the width of the wider ribbon (the unrolled outer tube), thus taking into account the effect of curvature on the registry mismatch between the two layers. Finally, circles are assigned to each atomic position on the two layers and the RI is calculated by using the procedure defined for the relevant planar system (*h*-BN in this case) at different interlayer

© 2013 Wiley-VCH Verlag GmbH & Co. KGaA, Weinheim

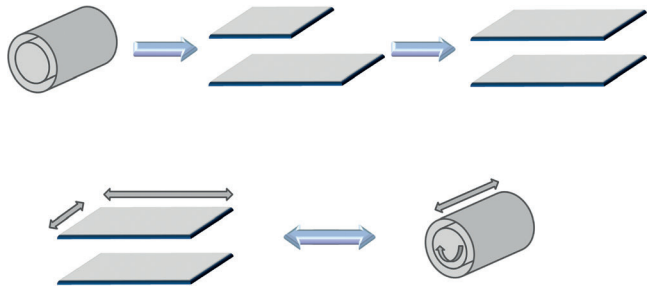

Figure 14. Representation of the procedure for the calculation of the RI of double-walled nanotubes: First, the two layers are unrolled. Next, the narrower ribbon (inner layer) is stretched to match the width of the wider ribbon (outer layer). Finally, circles are placed around the atomic positions and the RI is calculated for different relative positions of the unrolled layers, which are equivalent to the relative telescoping and rotation of the tubular bilayer system. Figure reproduced with permission from ref. [14a].

shifts parallel to the basal planes of the two layers. The resulting RI surface corresponds to relative telescoping and rotation of the two tube walls.

The performance of the RI method for tubular bilayers can be evaluated by comparing the RI sliding surface to results of DFT calculations for DWBNNTs with small unit cells. Thus, a set of DFT calculations was performed by using the local spin density (LSDA), PBE, and HSE exchange-correlation functional approximations with the 6-31G** basis set.[14a] Because the interlayer distance is fixed by the tube diameters in the case of DWNTs, the effects of dispersion interactions on the interlayer sliding energy, which have been shown to be of minor importance in *h*-BN[17] and in graphene,[29] were neglected throughout these calculations.

The results for a double-walled boron-nitride nanotube with a (5,5) inner shell and a (10,10) outer shell are presented in Figure 15. The tube was formed by rolling two AA′-stacked layers, whilst fixing the B–N distance to be about 1.44 Å. No geometry optimization was performed. The resulting inter-tube distance is about 3.44 Å, which is close to the equilibrium interlayer distance in *h*-BN (3.33 Å).[30] The rotation-telescoping energy landscape as obtained at the PBE/6-31G** level of theory is presented in Figure 15, top left. Similar results are obtained by using the LSDA and HSE functionals (not shown). The interlayer potential energy is much more sensitive towards the relative rotations of the two armchair nanotubes than to axial telescoping. The corrugation energy, which is defined as the maximal amplitude of the energy changes between different relative interlayer positions, is about 0.02 eV/unit cell. The corresponding RI surface, as shown in the Figure 15, bottom right, reproduces all of these effects whilst also capturing fine details of the energy landscape that was calculated from first principles.

Because the various layers of a multi-walled nanotube may differ in chirality, these systems present a rich variety of possible structures that can exhibit considerably different tribological properties. We emphasize that, similar to the results presented above for the armchair case, the RI is able to capture the inter-wall sliding-energy landscape of other DWBNNTs with various diameters and chiralities.[14a,31] This result further confirms the generality of the RI concept, which is not limited to

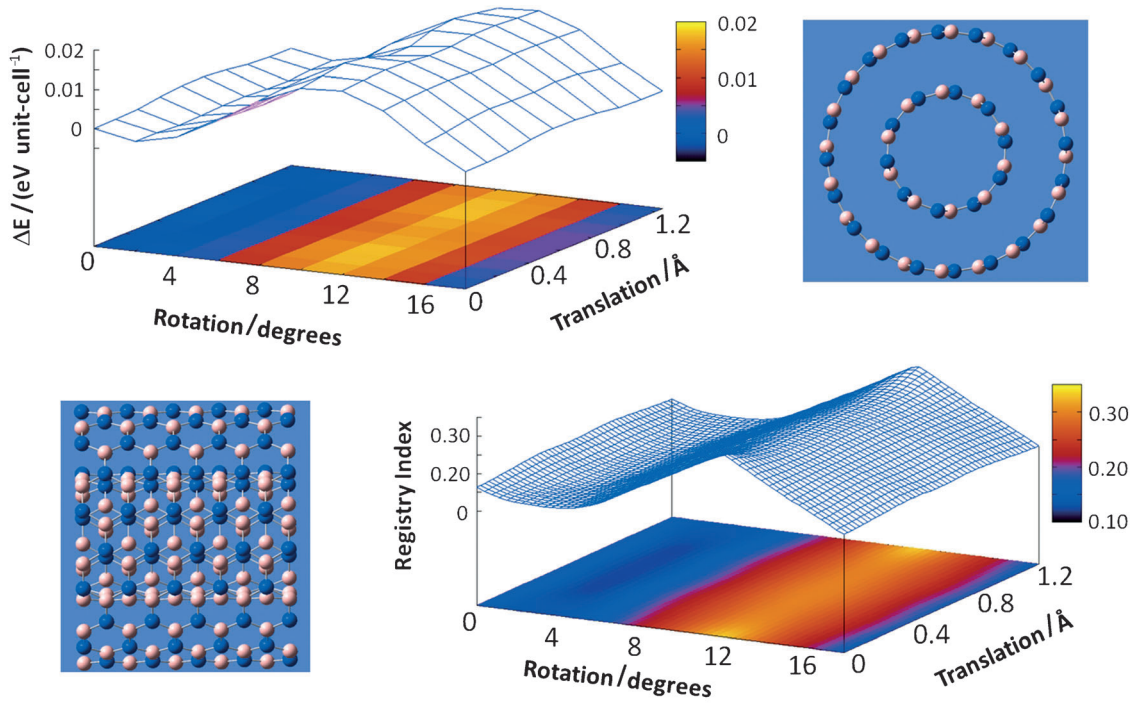

Figure 15. Rotation-telescoping-energy landscape of a (5,5)@(10,10) armchair DWBNNT. Top left: Relative total energies of different inter-tube configurations, as calculated by using DFT at the PBE/6-31G** level of theory. Bottom right: RI surface, as calculated by using the procedure described in the text. Axial and side views of the system are shown to emphasize the effects of curvature on the registry mismatch between the two tubes. Figure reproduced with permission from ref. [14a].

© 2013 Wiley-VCH Verlag GmbH & Co. KGaA, Weinheim

planar layered structures and can also be applied to systems that contain a finite curvature.

8. Summary and Outlook

As demonstrated throughout this review, the RI is a conceptually simple and computationally efficient tool for quantifying the degree of lattice commensurability in rigid nanoscale interfaces and for characterizing their sliding-energy landscape. This was shown by defining the RI for a hierarchy of materials junctions, including a mono-atomic graphene bilayer, a bi-atomic *h*-BN bilayer, a molybdenum disulfide bilayer having a complex sublayer structure, a heterogeneous junction of graphene and *h*-BN, and a double-walled boron-nitride nanotube that has a finite curvature. Furthermore, the intimate relation between the sliding-energy landscape and the tribological properties of rigid nanoscale interfaces allowed the RI to capture—down to fine details—the experimentally measured frictional behavior of a graphene flake sliding atop a graphite surface.

The success of the RI concept stems from the short-range nature of the interactions that determine the corrugation of the sliding-energy landscape of rigid interfaces. During the sliding process, the changes in the relative energetic stability of different inter-surface configurations result from variations in the repulsions between intercrossing electron densities of the two surfaces. Because the latter values are often proportional to the degree of overlap between localized electron clouds, they can be readily captured by geometrical considerations that incorporate the specific locations of the various atomic sites.

Based on this understanding, several directions along which the RI concept may be generalized can be envisioned. First, all of the interfaces that have been discussed in this Review involve parallel surfaces. The case of non-parallel interfaces, such as the rolling of carbon nanotubes on flat surfaces,[34] is common in nano-electromechanical systems. The short-range nature of the relevant interactions suggests that, in this case, one should only consider neighboring atomic sites of the different surfaces, thus considerably decreasing the dimensionality of the problem. Next, the effect of defects, such as vacancies or Stone–Wales defects, in the pristine lattice structure can be considered. Furthermore, the method is not limited to the description of layered materials. Studying the sliding-energy landscape of rigid bulk interfaces, such as nickel/nickel, palladium/palladium, and MoO_3/MoS_2 junctions, may be an excellent test case for evaluating the performance of the RI concept for such systems.[4au,5g,h] Another promising route to pursue is the characterization of molecular motion on surfaces.[32] Surface diffusion and driven motion of physisorbed molecules is of great relevance to the fields of chemical catalysis, chemical sensing, self-assembly, and nano-machining. The diffusive motion of an adsorbed molecule is dominated by the potential-energy landscape that it experiences as it slides along the surface,[33] which may be efficiently captured by defining an appropriate RI. Finally, the calculated RI surfaces may serve as an input for molecular dynamics simulations that, in turn, can be used to evaluate the dynamic aspects of the sliding process. Work along these lines is currently being pursued.

With the demonstrated success of the RI concept in describing the tribological properties of nanoscale interfaces and the wide range of possible extensions that may have impact on a variety of fields, such as catalysis, sensing, and self-assembly, it is hoped that the RI will become a standard part of the diverse simulation toolbox that is available to scientists in the field of nanotribology.

Acknowledgements

The author wishes to thank Prof. Helmut Schwarz for the encouragement and support in writing this review article and Prof. Michael Urbakh, Prof. Ernesto Joselevich, and Prof. Leeor Kronik for many insightful discussions on the subject of nanotribology. Many thanks to Hillel Kleiner for contributing his time and talent in preparing the frontispiece figure. This work was supported by the Israel Science Foundation under Grant No. 1313/08, the Center for Nanoscience and Nanotechnology at Tel Aviv University, the Israeli Ministry of Defense, and the Lise Meitner-Minerva Center for Computational Quantum Chemistry. The research leading to some of the presented results has received funding from the European Community's Seventh Framework Programme FP7/2007-2013 under Grant Agreement No. 249225.

Keywords: friction · interfaces · layered materials · molecular modeling · superlubricity

[1] a) S. H. Kim, D. B. Asay, M. T. Dugger, *Nano Today* **2007**, *2*, 22–29; b) J. Gao, W. D. Luedtke, U. Landman, *Phys. Rev. Lett.* **1997**, *79*, 705; c) S. Granick, *Science* **1991**, *253*, 1374–1379; d) J. N. Israelachvili, P. M. McGuiggan, A. M. Homola, *Science* **1988**, *240*, 189–191; e) J. Klein, E. Kumacheva, *J. Chem. Phys.* **1998**, *108*, 6996; f) U. Raviv, P. Laurat, J. Klein, *Nature* **2001**, *413*, 51–54; g) C. L. Rhykerd, M. Schoen, D. J. Diestler, J. H. Cushman, *Nature* **1987**, *330*, 461–463; h) P. A. Thompson, M. O. Robbins, G. S. Grest, *Isr. J. Chem.* **1995**, *35*, 93–106.

[2] a) B. Bhushan, J. N. Israelachvili, U. Landman, *Nature* **1995**, *374*, 607–616; b) O. M. Braun, A. G. Naumovets, *Surf. Sci. Rep.* **2006**, *60*, 79–158; c) E. Liu, B. Blanpain, J.-P. Celis, J. R. Roos, *J. Appl. Phys.* **1998**, *84*, 4859–4865; d) L. D. Marks, O. L. Warren, A. M. Minor, A. P. Merkle, *MRS Bull.* **2008**, *33*, 1168–1173; e) M. Nosonovsky, B. Bhushan, *Mater. Sci. Eng.* **2007**, *58*, 162–193; f) M. Urbakh, J. Klafter, D. Gourdon, J. Israelachvili, *Nature* **2004**, *430*, 525–528.

[3] a) R. Greenberg, G. Halperin, I. Etsion, R. Tenne, *Tribol. Lett.* **2004**, *17*, 179–186; b) L. Rapoport, Y. Bilik, Y. Feldman, M. Homyonfer, S. R. Cohen, R. Tenne, *Nature* **1997**, *387*, 791–793; c) L. Rapoport, Y. Feldman, M. Homyonfer, H. Cohen, J. Sloan, J. L. Hutchison, R. Tenne, *Wear* **1999**, *225–229*, 975–982; d) L. Rapoport, N. Fleischer, R. Tenne, *Adv. Mater.* **2003**, *15*, 651–655; e) L. Rapoport, N. Fleischer, R. Tenne, *J. Mater. Chem.* **2005**, *15*, 1782–1788; f) L. Rapoport, V. Leshchinsky, I. Lapsker, Y. Volovik, O. Nepomnyashchy, M. Lvovsky, R. Popovitz-Biro, Y. Feldman, R. Tenne, *Wear* **2003**, *255*, 785–793; g) L. Rapoport, V. Leshchinsky, M. Lvovsky, I. Lapsker, Y. Volovik, Y. Feldman, R. Popovitz-Biro, R. Tenne, *Wear* **2003**, *255*, 794–800; h) L. Rapoport, O. Nepomnyashchy, I. Lapsker, A. Verdyan, Y. Soifer, R. Popovitz-Biro, R. Tenne, *Tribol. Lett.* **2005**, *19*, 143–149; i) L. Cizaire, B. Vacher, T. Le Mogne, J. M. Martin, L. Rapoport, A. Margolin, R. Tenne, *Surf. Coat. Technol.* **2002**, *160*, 282–287; j) S. R. Cohen, Y. Feldman, H. Cohen, R. Tenne, *Appl. Surf. Sci.* **1999**, *144–145*, 603–607; k) S. R. Cohen, L. Rapoport, E. A. Ponomarev, H. Cohen, T. Tsirlina, R. Tenne, C. Lévy-Clément, *Thin Solid Films* **1998**, *324*, 190–197; l) Y. Golan, C. Drummond, M. Homyonfer, Y. Feldman, R. Tenne, J. Israelachvili, *Adv. Mater.* **1999**, *11*, 934–937; m) V. Leshchinsky, R. Popovitz-Biro, K.

© 2013 Wiley-VCH Verlag GmbH & Co. KGaA, Weinheim

Gartsman, R. Rosentsveig, Y. Rosenberg, R. Tenne, L. Rapoport, *J. Mater. Sci.* **2004**, *39*, 4119 – 4129; n) L. Rapoport, V. Leshchinsky, M. Lvovsky, O. Nepomnyashchy, Y. Volovik, R. Tenne, *Ind. Lubr. Tribol.* **2002**, *54*, 171 – 176; o) R. Rosentsveig, A. Gorodnev, N. Feuerstein, H. Friedman, A. Zak, N. Fleischer, J. Tannous, F. Dassenoy, R. Tenne, *Tribol. Lett.* **2009**, *36*, 175 – 182; p) R. Rosentsveig, A. Margolin, A. Gorodnev, R. Popovitz-Biro, Y. Feldman, L. Rapoport, Y. Novema, G. Naveh, R. Tenne, *J. Mater. Chem.* **2009**, *19*, 4368 – 4374.

[4] a) M. Dienwiebel, E. d. Kuyper, L. Crama, J. W. M. Frenken, J. A. Heimberg, D.-J. Spaanderman, D. G. v. Loon, T. Zijlstra, E. v. d. Drift, *Rev. Sci. Instrum.* **2005**, *76*, 043704; b) S. Korres, *Rev. Sci. Instrum.* **2010**, *81*, 063904; c) E. Gnecco, R. Bennewitz, T. Gyalog, E. Meyer, *J. Phys. Condens. Matter* **2001**, *13*, R619; d) H. Hölscher, A. Schirmeisen, U. D. Schwarz, *Philos. Trans. R. Soc. A* **2008**, *366*, 1383 – 1404; e) A. Schirmeisen, U. D. Schwarz, *ChemPhysChem* **2009**, *10*, 2373 – 2382; f) F. J. Giessibl, M. Herz, J. Mannhart, *Proc. Natl. Acad. Sci. USA* **2002**, *99*, 12006 – 12010; g) E. Gnecco, R. Bennewitz, T. Gyalog, C. Loppacher, M. Bammerlin, E. Meyer, H. J. Guntherodt, *Phys. Rev. Lett.* **2000**, *84*, 1172; h) A. Schirmeisen, L. Jansen, H. Fuchs, *Phys. Rev. B* **2005**, *71*, 245403; i) A. Socoliuc, R. Bennewitz, E. Gnecco, E. Meyer, *Phys. Rev. Lett.* **2004**, *92*, 134301; j) G. Binnig, C. F. Quate, C. Gerber, *Phys. Rev. Lett.* **1986**, *56*, 930; k) R. W. Carpick, M. Salmeron, *Chem. Rev.* **1997**, *97*, 1163 – 1194; l) J. S. Choi, J.-S. Kim, I.-S. Byun, D. H. Lee, M. J. Lee, B. H. Park, C. Lee, D. Yoon, H. Cheong, K. H. Lee, Y.-W. Son, J. Y. Park, M. Salmeron, *Science* **2011**, *333*, 607 – 610; m) G. Conache, S. M. Gray, A. Ribayrol, L. E. Fröberg, L. Samuelson, L. Montelius, H. Pettersson, *J. Appl. Phys.* **2010**, *108*, 094307; n) D. Dietzel, M. Feldmann, C. Herding, U. Schwarz, A. Schirmeisen, *Tribol. Lett.* **2010**, *39*, 273 – 281; o) D. Dietzel, T. Mönninghoff, L. Jansen, H. Fuchs, C. Ritter, U. D. Schwarz, A. Schirmeisen, *J. Appl. Phys.* **2007**, *102*, 084306; p) D. Dietzel, T. Monninghoff, C. Herding, M. Feldmann, H. Fuchs, B. Stegemann, C. Ritter, U. D. Schwarz, A. Schirmeisen, *Phys. Rev. B* **2010**, *82*, 035401; q) D. Dietzel, C. Ritter, T. Mnninghoff, H. Fuchs, A. Schirmeisen, U. D. Schwarz, *Phys. Rev. Lett.* **2008**, *101*, 125505; r) Y. Enomoto, D. Tabor, *Proc. R. Soc. A* **1981**, *373*, 405 – 417; s) A. E. Filippov, M. Dienwiebel, J. W. M. Frenken, J. Klafter, M. Urbakh, *Phys. Rev. Lett.* **2008**, *100*, 046102; t) T. Filleter, R. Bennewitz, *Phys. Rev. B* **2010**, *81*, 155412; u) T. Filleter, J. L. McChesney, A. Bostwick, E. Rotenberg, K. V. Emtsev, T. Seyller, K. Horn, R. Bennewitz, *Phys. Rev. Lett.* **2009**, *102*, 086102; v) J. Fineberg, *Nat. Mater.* **2011**, *10*, 3 – 4; w) C. D. Frisbie, L. F. Rozsnyai, A. Noy, M. S. Wrighton, C. M. Lieber, *Science* **1994**, *265*, 2071 – 2074; x) S. Fujisawa, Y. Sugawara, S. Ito, S. Mishima, T. Okada, S. Morita, *Nanotechnology* **1993**, *4*, 138; y) S. Fujisawa, E. Kishi, Y. Sugawara, S. Morita, *Phys. Rev. B* **1995**, *52*, 5302; z) S. Fujisawa, E. Kishi, Y. Sugawara, S. Morita, *Phys. Rev. B* **1995**, *51*, 7849; aa) G. J. Germann, S. R. Cohen, G. Neubauer, G. M. McClelland, H. Seki, D. Coulman, *J. Appl. Phys.* **1993**, *73*, 163 – 167; ab) H. Hedgeland, P. Fouquet, A. P. Jardine, G. Alexandrowicz, W. Allison, J. Ellis, *Nat. Phys.* **2009**, *5*, 561 – 564; ac) J. Hu, X. d. Xiao, D. F. Ogletree, M. Salmeron, *Surf. Sci.* **1995**, *327*, 358 – 370; ad) H. Lee, N. Lee, Y. Seo, J. Eom, S. Lee, *Nanotechnology* **2009**, *20*, 325701; ae) S. Kamiya, D. Tsuda, K. Miura, N. Sasaki, *Wear* **2004**, *257*, 1133 – 1136; af) R. Kaneko, K. Nonaka, K. Yasuda, *J. Vac. Sci. Technol. A* **1988**, *6*, 291 – 292; ag) T. Koch, M. Evaristo, A. Pauschitz, M. Roy, A. Cavaleiro, *Thin Solid Films* **2009**, *518*, 185 – 193; ah) M. A. Lantz, S. J. O'Shea, M. E. Welland, K. L. Johnson, *Phys. Rev. B* **1997**, *55*, 10776; ai) R. Lüthi, E. Meyer, H. Haefke, L. Howald, W. Gutmannsbauer, H.-J. Güntherodt, *Science* **1994**, *266*, 1979 – 1981; aj) S. Maier, E. Gnecco, A. Baratoff, R. Bennewitz, E. Meyer, *Phys. Rev. B* **2008**, *78*, 045432; ak) J. M. Martin, C. Donnet, T. Le Mogne, T. Epicier, *Phys. Rev. B* **1993**, *48*, 10583; al) C. M. Mate, G. M. McClelland, R. Erlandsson, S. Chiang, *Phys. Rev. Lett.* **1987**, *59*, 1942; am) A. P. Merkle, L. D. Marks, *Appl. Phys. Lett.* **2007**, *90*, 064101; an) K. Miura, S. Kamiya, *Europhys. Lett.* **2002**, *58*, 610; ao) S. Morita, S. Fujisawa, Y. Sugawara, *Surf. Sci. Rep.* **1996**, *23*, 1 – 41; ap) J. Y. Park, D. F. Ogletree, M. Salmeron, R. A. Ribeiro, P. C. Canfield, C. J. Jenks, P. A. Thiel, *Science* **2005**, *309*, 1354 – 1356; aq) J. Y. Park, D. F. Ogletree, M. Salmeron, R. A. Ribeiro, P. C. Canfield, C. J. Jenks, P. A. Thiel, *Phys. Rev. B* **2005**, *71*, 144203; ar) C. Ritter, M. Heyde, B. Stegemann, K. Rademann, U. D. Schwarz, *Phys. Rev. B* **2005**, *71*, 085405; as) J. A. Ruan, B. Bhushan, *J. Appl. Phys.* **1994**, *76*, 5022 – 5035; at) U. D. Schwarz, O. Zwrner, P. Koster, R. Wiesendanger, *Phys. Rev. B* **1997**, *56*, 6987; au) P. E. Sheehan, C. M. Lieber, *Science* **1996**, *272*, 1158 – 1161; av) P. Steiner, E. Gnecco, T. Filleter, N. Gosvami, S. Maier, E. Meyer, R. Bennewitz, *Tribol. Lett.* **2010**, *39*, 321 – 327; aw) J. Tamayo, R. García, T. Utzmeier, F. Briones, *Phys. Rev. B* **1997**, *55*, R13436 – R13439; ax) M. Ternes, C. P. Lutz, C. F. Hirjibehedin, F. J. Giessibl, A. J. Heinrich, *Science* **2008**, *319*, 1066 – 1069; ay) A. Tomala, M. Roy, F. Franek, *Philos. Mag.* **2010**, *90*, 3827 – 3843; az) E. Tranvouez, A. Orieux, E. Boer-Duchemin, C. H. Devillers, V. Huc, G. Comtet, G. Dujardin, *Nanotechnology* **2009**, *20*, 165304; ba) J. Wang, K. C. Rose, C. M. Lieber, *J. Phys. Chem. B* **1999**, *103*, 8405 – 8409; bb) Y. P. Jeong, D. F. Ogletree, M. Salmeron, R. A. Ribeiro, P. C. Canfield, C. J. Jenks, P. A. Thiel, *Phys. Rev. B* **2006**, *74*, 024203.

[5] a) M. Dienwiebel, G. S. Verhoeven, N. Pradeep, J. W. M. Frenken, J. A. Heimberg, H. W. Zandbergen, *Phys. Rev. Lett.* **2004**, *92*, 126101; b) M. Hirano, K. Shinjo, *Phys. Rev. B* **1990**, *41*, 11837; c) K. Shinjo, M. Hirano, *Surf. Sci.* **1993**, *283*, 473 – 478; d) M. R. Sørensen, K. W. Jacobsen, P. Stoltze, *Phys. Rev. B* **1996**, *53*, 2101; e) M. Hirano, K. Shinjo, R. Kaneko, Y. Murata, *Phys. Rev. Lett.* **1991**, *67*, 2642; f) M. Hirano, K. Shinjo, R. Kaneko, Y. Murata, *Phys. Rev. Lett.* **1997**, *78*, 1448; g) J. S. Ko, A. J. Gellman, *Langmuir* **2000**, *16*, 8343 – 8351; h) C. M. Mancinelli, A. J. Gellman, *Langmuir* **2004**, *20*, 1680 – 1687; i) T. Liang, W. G. Sawyer, S. S. Perry, S. B. Sinnott, S. R. Phillpot, *Phys. Rev. B* **2008**, *77*, 104105; j) N. Manini, O. M. Braun, *Phys. Lett. A* **2011**, *375*, 2946 – 2951; k) A. P. Merkle, L. D. Marks, *Philos. Mag. Lett.* **2007**, *87*, 527 – 532; l) G. E. Santoro, A. Vanossi, N. Manini, G. Divitini, E. Tosatti, *Surf. Sci.* **2006**, *600*, 2726 – 2729; m) J. B. Sokoloff, *Phys. Rev. B* **1990**, *42*, 760; n) M. Weiss, F.-J. Elmer, *Phys. Rev. B* **1996**, *53*, 7539.

[6] a) E. Gnecco, A. Socoliuc, S. Maier, J. Gessler, T. Glatzel, A. Baratoff, E. Meyer, *Nanotechnology* **2009**, *20*, 025501; b) M. A. Lantz, D. Wiesmann, B. Gotsmann, *Nat. Nanotechnol.* **2009**, *4*, 586 – 591; c) J. Frenken, *Nat. Nanotechnol.* **2006**, *1*, 20 – 21; d) A. Socoliuc, E. Gnecco, S. Maier, O. Pfeiffer, A. Baratoff, R. Bennewitz, E. Meyer, *Science* **2006**, *313*, 207 – 210; e) P. Steiner, R. Roth, E. Gnecco, A. Baratoff, S. Maier, T. Glatzel, E. Meyer, *Phys. Rev. B* **2009**, *79*, 045414; f) H. Iizuka, J. Nakamura, A. Natori, *Phys. Rev. B* **2009**, *80*, 155449; g) V. Zaloj, M. Urbakh, J. Klafter, *Phys. Rev. Lett.* **1999**, *82*, 4823.

[7] M. Dienwiebel, N. Pradeep, G. S. Verhoeven, H. W. Zandbergen, J. W. M. Frenken, *Surf. Sci.* **2005**, *576*, 197 – 211.

[8] a) E. Gnecco, S. Maier, E. Meyer, *J. Phys. Condensed Matter* **2008**, *20*, 354004; b) G. S. Verhoeven, M. Dienwiebel, J. W. M. Frenken, *Phys. Rev. B* **2004**, *70*, 165418.

[9] a) K. S. Nagapriya, O. Goldbart, I. Kaplan-Ashiri, G. Seifert, R. Tenne, E. Joselevich, *Phys. Rev. Lett.* **2008**, *101*, 195501; b) T. Cohen-Karni, L. Segev, O. Srur-Lavi, S. R. Cohen, E. Joselevich, *Nat. Nanotechnol.* **2006**, *1*, 36 – 41; c) C. Stampfer, A. Jungen, R. Linderman, D. Obergfell, S. Roth, C. Hierold, *Nano Lett.* **2006**, *6*, 1449 – 1453; d) A. M. Fennimore, T. D. Yuzvinsky, W.-Q. Han, M. S. Fuhrer, J. Cumings, A. Zettl, *Nature* **2003**, *424*, 408 – 410; e) H. B. Peng, C. W. Chang, S. Aloni, T. D. Yuzvinsky, A. Zettl, *Phys. Rev. Lett.* **2006**, *97*, 087203; f) Q. Zheng, Q. Jiang, *Phys. Rev. Lett.* **2002**, *88*, 045503; g) J. Cumings, A. Zettl, *Science* **2000**, *289*, 602 – 604; h) L. Forró, *Science* **2000**, *289*, 560 – 561; i) D. S. Grierson, R. W. Carpick, *Nano Today* **2007**, *2*, 12 – 21; j) J. S. Bunch, A. M. van der Zande, S. S. Verbridge, I. W. Frank, D. M. Tanenbaum, J. M. Parpia, H. G. Craighead, P. L. McEuen, *Science* **2007**, *315*, 490 – 493.

[10] a) G. A. Tomlinson, *Philos. Mag.* **1929**, *7*, 905 – 939; b) C. Daly, J. Zhang, J. B. Sokoloff, *Phys. Rev. Lett.* **2003**, *90*, 246101; c) D. Tománek, W. Zhong, H. Thomas, *Europhys. Lett.* **1991**, *15*, 887; d) T. Gyalog, M. Bammerlin, R. Lüthi, E. Meyer, H. Thomas, *Europhys. Lett.* **1995**, *31*, 269; e) T. Gyalog, H. Thomas, *Europhys. Lett.* **1997**, *37*, 195; f) O. K. Dudko, A. E. Filippov, J. Klafter, M. Urbakh, *Chem. Phys. Lett.* **2002**, *352*, 499 – 504; g) Q. Li, Y. Dong, D. Perez, A. Martini, R. W. Carpick, *Phys. Rev. Lett.* **2011**, *106*, 126101; h) S. Maier, Y. Sang, T. Filleter, M. Grant, R. Bennewitz, E. Gnecco, E. Meyer, *Phys. Rev. B* **2005**, *72*, 245418; i) S. Y. Krylov, J. W. M. Frenken, *J. Phys. Condens. Matter* **2008**, *20*, 354003; j) L. Prandtl, *ZAMM J. Appl. Math. Mech.* **1928**, *8*, 85 – 106; k) L. Mai-Mai, *Phys. Scr.* **2010**, *82*, 025005; l) C.-L. Wang, W.-S. Duan, Y. Yang, J.-M. Chen, *Commun. Theor. Phys.* **2010**, *54*, 112; m) D. G. Abel, S. Y. Krylov, J. W. M. Frenken, *Phys. Rev. Lett.* **2007**, *99*, 166102; n) E. Boer-Duchemin, E. Tranvouez, G. Dujardin, *Nanotechnology* **2010**, *21*, 455704; o) C. Campañá, *Phys. Rev. B* **2007**, *75*, 155419; p) L. Consoli, H. J. F. Knops, A. Fasolino, *Phys. Rev. Lett.* **2000**, *85*, 302; q) A. de Wijn, A. Fasolino, *Tribol. Lett.* **2010**, *39*, 91 – 99; r) A. S. de Wijn, C. Fusco, A. Fasolino, *Phys. Rev. E* **2010**, *81*, 046105; s) D. J. Diestler, E. Rajasekaran, X. C. Zeng, *J. Phys. Chem. B* **1997**, *101*, 4992 – 4997; t) E. Gnecco, *Europhys. Lett.* **2010**, *91*, 66008; u) A. E. Fili-

© 2013 Wiley-VCH Verlag GmbH & Co. KGaA, Weinheim

ppov, A. Vanossi, M. Urbakh, *Phys. Rev. E* **2009**, *79*, 021108; v) G. He, M. H. Müser, M. O. Robbins, *Science* **1999**, *284*, 1650 – 1652; w) G. He, M. O. Robbins, *Phys. Rev. B* **2001**, *64*, 035413; x) H. Hölscher, U. D. Schwarz, R. Wiesendanger, *Surf. Sci.* **1997**, *375*, 395 – 402; y) H. Hölscher, U. D. Schwarz, O. Zworner, R. Wiesendanger, *Phys. Rev. B* **1998**, *57*, 2477; z) J. N. Israelachvili, *Nature* **2005**, *435*, 893 – 895; aa) K. B. Jinesh, S. Y. Krylov, H. Valk, M. Dienwiebel, J. W. M. Frenken, *Phys. Rev. B* **2008**, *78*, 155440; ab) O. M. Braun, Y. S. Kivshar, *Phys. Rep.* **1998**, *306*, 1 – 108; ac) W. K. Kim, M. L. Falk, *Phys. Rev. B* **2009**, *80*, 235428; ad) S. Y. Krylov, J. A. Dijksman, W. A. van Loo, J. W. M. Frenken, *Phys. Rev. Lett.* **2006**, *97*, 166103; ae) S. Y. Krylov, J. W. M. Frenken, *Phys. Rev. B* **2009**, *80*, 235435; af) S. Y. Krylov, K. B. Jinesh, H. Valk, M. Dienwiebel, J. W. M. Frenken, *Phys. Rev. E* **2005**, *71*, 065101; ag) A. Merkle, L. Marks, *Tribol. Lett.* **2007**, *26*, 73 – 84; ah) M. H. Müser, *Europhys. Lett.* **2004**, *66*, 97; ai) M. H. Müser, L. Wenning, M. O. Robbins, *Phys. Rev. Lett.* **2001**, *86*, 1295; aj) J. B. Pendry, *J. Phys. Condens. Matter* **1997**, *9*, 10301; ak) S. Pisov, E. Tosatti, U. Tartaglino, A. Vanossi, *J. Phys.: Condensed Matter* **2007**, *19*, 305015; al) A. M. Popov, I. V. Lebedeva, A. A. Knizhnik, Y. E. Lozovik, B. V. Potapkin, *Phys. Rev. B* **2011**, *84*, 045404; am) M. G. Rozman, M. Urbakh, J. Klafter, *Phys. Rev. E* **1998**, *57*, 7340; an) Y. Sang, M. Dubé, M. Grant, *Phys. Rev. Lett.* **2001**, *87*, 174301; ao) S. Y. Krylov, J. W. M. Frenken, *New J. Phys.* **2007**, *9*, 398; ap) J. B. Sokoloff, *Surf. Sci.* **1984**, *144*, 267 – 272; aq) P. Steiner, R. Roth, E. Gnecco, A. Baratoff, E. Meyer, *Phys. Rev. B* **2010**, *82*, 205417; ar) U. Tartaglino, V. N. Samoilov, B. N. J. Persson, *J. Phys.: Condensed Matter* **2006**, *18*, 4143; as) A. Zmitrowicz, *Int. J. Solids Struct.* **2006**, *43*, 4407 – 4451.

[11] a) U. Landman, W. D. Luedtke, E. M. Ringer, *Wear* **1992**, *153*, 3 – 30; b) U. Landman, W. D. Luedtke, *J. Vac. Sci. Technol. B* **1991**, *9*, 414 – 423; c) F. Bonelli, N. Manini, E. Cadelano, L. Colombo, *Eur. Phys. J. B* **2009**, *70*, 449 – 459; d) Y. Dong, D. Perez, A. Voter, A. Martini, *Tribol. Lett.* **2011**, *42*, 99 – 107; e) P. Fouquet, M. R. Johnson, H. Hedgeland, A. P. Jardine, J. Ellis, W. Allison, *Carbon* **2009**, *47*, 2627 – 2639; f) B. Luan, M. O. Robbins, *Nature* **2005**, *435*, 929 – 932; g) T. Onodera, Y. Morita, R. Nagumo, R. Miura, A. Suzuki, H. Tsuboi, N. Hatakeyama, A. Endou, H. Takaba, F. Dassenoy, C. Minfray, L. Joly-Pottuz, M. Kubo, J.-M. Martin, A. Miyamoto, *J. Phys. Chem. B* **2010**, *114*, 15832 – 15838; h) T. Onodera, Y. Morita, A. Suzuki, M. Koyama, H. Tsuboi, N. Hatakeyama, A. Endou, H. Takaba, M. Kubo, F. Dassenoy, C. Minfray, L. Joly-Pottuz, J.-M. Martin, A. Miyamoto, *J. Phys. Chem. B* **2009**, *113*, 16526 – 16536; i) L. Vitos, K. Larsson, B. Johansson, M. Hanson, S. Hogmark, *Comput. Mater. Sci.* **2006**, *37*, 193 – 197; j) P. Depondt, A. Ghazali, J. C. S. Lévy, *Surf. Sci.* **1998**, *419*, 29 – 37; k) J. N. Glosli, G. M. McClelland, *Phys. Rev. Lett.* **1993**, *70*, 1960; l) R. Guerra, U. Tartaglino, A. Vanossi, E. Tosatti, *Nat. Mater.* **2010**, *9*, 634 – 637; m) Y. Guo, W. Guo, C. Chen, *Phys. Rev. B* **2007**, *76*, 155429; n) J. A. Harrison, C. T. White, R. J. Colton, D. W. Brenner, *Phys. Rev. B* **1992**, *46*, 9700; o) N. Itamura, K. Miura, N. Sasaki, *Jpn. J. Appl. Phys.* **2009**, *48*, 060207; p) A. V. Khomenko, N. V. Prodanov, *Carbon* **2010**, *48*, 1234 – 1243; q) X. Liang, T. B. Ma, Y. Z. Hu, H. Wang, *Nanotechnology* **2011**, *22*, 285708; r) K. Miura, N. Sasaki, S. Kamiya, *Phys. Rev. B* **2004**, *69*, 075420; s) K. Mylvaganam, L. C. Zhang, *J. Comput. Theor. Nanosci.* **2010**, *7*, 2199 – 2202; t) N. Sasaki, K. Kobayashi, M. Tsukada, *Phys. Rev. B* **1996**, *54*, 2138; u) A. L. Shluger, A. L. Rohl, R. T. Williams, R. M. Wilson, *Phys. Rev. B* **1995**, *52*, 11398; v) W. Zhong, D. Tomanek, *Phys. Rev. Lett.* **1990**, *64*, 3054; w) T. Zykova-Timan, D. Ceresoli, E. Tosatti, *Nat. Mater.* **2007**, *6*, 230 – 234.

[12] Y. I. Frenkel, T. A. Kontorova, *Zh. Eksp. Teor. Fiz.* **1938**, *8*, 89.

[13] a) M. H. Müser *Theoretical Aspects of Superlubricity in Fundamentals of Friction and Wear on the Nanoscale* (Eds.: E. Gnecco, E. Meyer), Springer, Berlin, Heidelberg, **2007**, pp. 177 – 199; b) M. H. Müser, M. Urbakh, M. O. Robbins in *Advances in Chemical Physics*, Wiley, Hoboken, **2003**, pp. 187 – 272; c) H.-J. Kim, D.-E. Kim, *Int. J. Precision Eng. Manufacturing* **2009**, *10*, 141 – 151; d) M. O. Robbins, M. H. Muser in *Modern Tribology Handbook* (Ed.: B. Bhushan), CRC, Boca Raton, **2001**, pp. 717 – 765; e) N. Sasaki, N. Itamura, D. Tsuda, K. Miura, *Curr. Nanosci.* **2007**, *3*, 105 – 115; f) N. Sasaki, M. Tsukada, S. Fujisawa, Y. Sugawara, S. Morita, K. Kobayashi, *Phys. Rev. B* **1998**, *57*, 3785; g) I. L. Singer, *J. Vac. Sci. Technol. A* **1994**, *12*, 2605 – 2616.

[14] a) O. Hod, *Isr. J. Chem.* **2010**, *50*, 506 – 514; b) O. Hod, *Phys. Rev. B* **2012**, *86*, 075444.

[15] C. Zhang, *J. Phys. Chem. B* **2007**, *111*, 6208 – 6213.

[16] A. Carlson, T. Dumitrică, *Nanotechnology* **2007**, *18*, 065706.

[17] N. Marom, J. Bernstein, J. Garel, A. Tkatchenko, E. Joselevich, L. Kronik, O. Hod, *Phys. Rev. Lett.* **2010**, *105*, 046801.

[18] a) T. Kuzuba, T. Sato, T. Ishii, T. Arai, *Phys. Rev. B* **1985**, *32*, 1230; b) N. Ooi, A. Rairkar, L. Lindsley, J. B. Adams, *J. Phys. Condens. Matter* **2006**, *18*, 97; c) Y. Qi, J. L. G. Hector, *Appl. Phys. Lett.* **2007**, *90*, 081922 – 081923; d) L. Liu, Y. P. Feng, Z. X. Shen, *Phys. Rev. B* **2003**, *68*, 104102; e) S. Yamamura, M. Takata, M. Sakata, *J. Phys. Chem. Solids* **1997**, *58*, 177 – 183; f) A. Catellani, M. Posternak, A. Baldereschi, A. J. Freeman, *Phys. Rev. B* **1987**, *36*, 6105; g) Y. Muramatsu, T. Kaneyoshi, E. M. Gullikson, R. C. C. Perera, *Spectrochim. Acta Part A* **2003**, *59*, 1951 – 1957; h) O. Hod, *J. Chem. Theory Comput.* **2012**, *8*, 1360 – 1369.

[19] a) J. P. Perdew, K. Burke, M. Ernzerhof, *Phys. Rev. Lett.* **1996**, *77*, 3865 – 3868; b) J. P. Perdew, K. Burke, M. Ernzerhof, *Phys. Rev. Lett.* **1997**, *78*, 1396 – 1396.

[20] a) A. Tkatchenko, M. Scheffler, *Phys. Rev. Lett.* **2009**, *102*, 073005; b) N. Marom, A. Tkatchenko, M. Scheffler, L. Kronik, *J. Chem. Theory Comput.* **2010**, *6*, 81 – 90; c) N. Marom, A. Tkatchenko, M. Rossi, V. V. Gobre, O. Hod, M. Scheffler, L. Kronik, *J. Chem. Theory Comput.* **2011**, *7*, 3944 – 3951.

[21] A. Blumberg, U. Keshet, I. Zaltsman, O. Hod, *J. Phys. Chem. Lett.* **2012**, *3*, 1936 – 1940.

[22] S. Cahangirov, C. Ataca, M. Topsakal, H. Sahin, S. Ciraci, *Phys. Rev. Lett.* **2012**, *108*, 126103.

[23] A. S. de Wijn, A. Fasolino, A. E. Filippov, M. Urbakh, *Europhys. Lett.* **2011**, *95*, 66002.

[24] I. Leven, D. Krepel, O. Shemesh, O. Hod, *J. Phys. Chem. Lett.* **2013**, *4*, 115 – 120.

[25] a) G. Giovannetti, P. A. Khomyakov, G. Brocks, P. J. Kelly, J. van den Brink, *Phys. Rev. B* **2007**, *76*, 073103; b) C. R. Dean, A. F. Young, I. Meric, C. Lee, L. Wang, S. Sorgenfrei, K. Watanabe, T. Taniguchi, P. Kim, K. L. Shepard, J. Hone, *Nat. Nanotechnol.* **2010**, *5*, 722 – 726; c) J. Slawinska, I. Zasada, Z. Klusek, *Phys. Rev. B* **2010**, *81*, 155433; d) J. Sławinska, I. Zasada, P. Kosinski, Z. Klusek, *Phys. Rev. B* **2010**, *82*, 085431; e) X. Ding, G. Ding, X. Xie, F. Huang, M. Jiang, *Carbon* **2011**, *49*, 2522 – 2525; f) Y. Fan, M. Zhao, Z. Wang, X. Zhang, H. Zhang, *Appl. Phys. Lett.* **2011**, *98*, 083103 – 083103; g) Z. Liu, L. Song, S. Zhao, J. Huang, L. Ma, J. Zhang, J. Lou, P. M. Ajayan, *Nano Lett.* **2011**, *11*, 2032 – 2037; h) B. Sachs, T. O. Wehling, M. I. Katsnelson, A. I. Lichtenstein, *Phys. Rev. B* **2011**, *84*, 195414; i) J. Xue, J. Sanchez-Yamagishi, D. Bulmash, P. Jacquod, A. Deshpande, K. Watanabe, T. Taniguchi, P. Jarillo-Herrero, B. J. LeRoy, *Nat. Mater.* **2011**, *10*, 282 – 285; j) M. Yankowitz, J. Xue, D. Cormode, J. D. Sanchez-Yamagishi, K. Watanabe, T. Taniguchi, P. Jarillo-Herrero, P. Jacquod, B. J. LeRoy, *Nat. Phys.* **2012**, *8*, 382 – 386; k) L. A. Ponomarenko, A. K. Geim, A. A. Zhukov, R. Jalil, S. V. Morozov, K. S. Novoselov, I. V. Grigorieva, E. H. Hill, V. V. Cheianov, V. I. Fal'ko, K. Watanabe, T. Taniguchi, R. V. Gorbachev, *Nat. Phys.* **2011**, *7*, 958 – 961; l) R. g. Decker, Y. Wang, V. W. Brar, W. Regan, H.-Z. Tsai, Q. Wu, W. Gannett, A. Zettl, M. F. Crommie, *Nano Lett.* **2011**, *11*, 2291 – 2295; m) I. Meric, C. Dean, A. Young, J. Hone, P. Kim, K. L. Shepard in *Tech. Digest Int. Electron Devices Meet.* **2010**, *10*, 556 – 559, **2010**, pp. 23.22.21 – 23.22.24.

[26] a) J. Heyd, G. E. Scuseria, M. Ernzerhof, *J. Chem. Phys.* **2003**, *118*, 8207 – 8215; b) J. Heyd, G. E. Scuseria, *J. Chem. Phys.* **2004**, *120*, 7274 – 7280; c) J. Heyd, G. E. Scuseria, *J. Chem. Phys.* **2004**, *121*, 1187 – 1192; d) J. Heyd, G. E. Scuseria, M. Ernzerhof, *J. Chem. Phys.* **2006**, *124*, 219906 – 219901.

[27] P. C. Hariharan, J. A. Pople, *Theor. Chem. Acc.* **1973**, *28*, 213 – 222.

[28] *Gaussian 09, Revision A.02*, M. J. Frisch, G. W. Trucks, H. B. Schlegel, G. E. Scuseria, M. A. Robb, J. R. Cheeseman, G. Scalmani, V. Barone, B. Mennucci, G. A. Petersson, H. Nakatsuji, M. Caricato, X. Li, H. P. Hratchian, A. F. Izmaylov, J. Bloino, G. Zheng, J. L. Sonnenberg, M. Hada, M. Ehara, K. Toyota, R. Fukuda, J. Hasegawa, M. Ishida, T. Nakajima, Y. Honda, O. Kitao, H. Nakai, T. Vreven, J. A. Montgomery, J. E. Peralta, F. Ogliaro, M. Bearpark, J. J. Heyd, E. Brothers, K. N. Kudin, V. N. Staroverov, R. Kobayashi, J. Normand, K. Raghavachari, A. Rendell, J. C. Burant, S. S. Iyengar, J. Tomasi, M. Cossi, N. Rega, J. M. Millam, M. Klene, J. E. Knox, J. B. Cross, V. Bakken, C. Adamo, J. Jaramillo, R. Gomperts, R. E. Stratmann, O. Yazyev, A. J. Austin, R. Cammi, C. Pomelli, J. W. Ochterski, R. L. Martin, K. Morokuma, V. G. Zakrzewski, G. A. Voth, P. Salvador, J. J. Dannenberg, S. Dapprich, A. D. Daniels, Farkas, J. B. Foresman, J. V. Ortiz, J. Cioslowski, D. J. Fox, Gaussian Inc., Wallingford CT, **2009**.

[29] A. N. Kolmogorov, V. H. Crespi, *Phys. Rev. B* **2005**, *71*, 235415.

© 2013 Wiley-VCH Verlag GmbH & Co. KGaA, Weinheim

[30] a) R. Pease, *Acta Crystallogr.* **1952**, *5*, 356 – 361; b) V. L. Solozhenko, G. Will, F. Elf, *Solid State Commun.* **1995**, *96*, 1 – 3; c) G. Kern, G. Kresse, J. Hafner, *Phys. Rev. B* **1999**, *59*, 8551; d) W. Paszkowicz, J. B. Pelka, M. Knapp, T. Szyszko, S. Podsiadlo, *Appl. Phys. A* **2002**, *75*, 431 – 435; e) A. Marini, P. Garcia-Gonzalez, A. Rubio, *Phys. Rev. Lett.* **2006**, *96*, 136404; f) Y. Shi, C. Hamsen, X. Jia, K. K. Kim, A. Reina, M. Hofmann, A. L. Hsu, K. Zhang, H. Li, Z.-Y. Juang, M. S. Dresselhaus, L.-J. Li, J. Kong, *Nano Lett.* **2010**, *10*, 4134 – 4139.

[31] J. Garel, I. Leven, C. Zhi, K. S. Nagapriya, R. Popovitz-Biro, D. Golberg, Y. Bando, O. Hod, E. Joselevich, *Nano Lett.* **2012**, *12*, 6347 – 6352.

[32] I. Calvo-Almazán, T. Seydel, P. Fouquet, *J. Phys. Condens. Matter* **2010**, *22*, 304014.

[33] a) I. V. Lebedeva, A. A. Knizhnik, A. M. Popov, O. V. Ershova, Y. E. Lozovik, B. V. Potapkin, *Phys. Rev. B* **2010**, *82*, 155460; b) I. V. Lebedeva, A. A. Knizhnik, A. M. Popov, O. V. Ershova, Y. E. Lozovik, B. V. Potapkin, *J. Chem. Phys.* **2011**, *134*, 104505; c) Q. Zheng, B. Jiang, S. Liu, Y. Weng, L. Lu, Q. Xue, J. Zhu, Q. Jiang, S. Wang, L. Peng, *Phys. Rev. Lett.* **2008**, *100*, 067205.

[34] a) M. R. Falvo, R. M. Taylor II, A. Helser, V. Chi, F. P. Brooks Jr., S. Washburn, R. Superfine, *Nature* **1999**, *397*, 236 – 238, b) M. Lucas, X. Zhang, I. Palaci, C. Klinke, E. Tosatti, E. Riedo, *Nature Materials* **2009**, *8*, 876 – 881, c) A. Buldum, J. P. Lu, *Phys. Rev. Lett.* **1999**, *83*, 5050 – 5053, d) J. D. Schall, D. W. Brenner, *Molecular Simulation* **2000**, *25*, 73 – 79.

Received: March 14, 2013
Published online on June 18, 2013

© 2013 Wiley-VCH Verlag GmbH & Co. KGaA, Weinheim